Impact melt rocks from the Late Paleocene Hiawatha impact structure, northwest Greenland

William R. HYDE [1]*, Adam A. GARDE [2], Nynke KEULEN [2], Sebastian N. MALKKI [2],
Steven J. JARET [3,4], Tod WAIGHT [5], Pierre BECK [6], Iain McDONALD [7], and
Nicolaj K. LARSEN [1]

[1]Globe Institute, University of Copenhagen, Copenhagen K, Denmark
[2]Geological Survey of Denmark and Greenland, Copenhagen K, Denmark
[3]Department of Earth and Planetary Sciences, American Museum of Natural History, New York, New York, USA
[4]Department of Physical Sciences, Kingsborough Community College, City University of New York, Brooklyn, New York, USA
[5]Department of Geosciences and Natural Resource Management (Geology Section), University of Copenhagen, Copenhagen K, Denmark
[6]Université Grenoble Alpes, CNRS, IPAG, Grenoble, France
[7]School of Earth and Environmental Sciences, Cardiff University, Cardiff, UK
*Corresponding author.
William R. Hyde, Globe Institute, University of Copenhagen, Øster Voldgade 5, 1350 Copenhagen K, Denmark.
E-mail: william.hyde@sund.ku.dk

Abstract–Impact melt rocks formed during hypervelocity impact events are ideal for studying impact structures. Here, we describe impact melt rock samples collected proximal to the 31 km wide 58 Ma Hiawatha impact structure, northwest Greenland, which is completely covered by the Greenland Ice Sheet. The melt rocks contain diagnostic shock indicators (e.g., planar deformation features [PDF] in quartz and shocked zircon) and form three groups based on melt textures and chemistry: (i) hypocrystalline, (ii) glassy, and (iii) carbonate-based melt rocks. The exposed foreland directly in front of the structure consists of metasedimentary successions and igneous plutons; however, the carbonate-based impactites indicate a mixed target sequence with a significant carbonate-rich component. Well-preserved organic material in some melt rocks indicates that North Greenland at the time of impact was host to abundant organic material, likely a dense high-latitude temperate forest. Geochemical signatures of platinum-group elements in selected samples indicate an extraterrestrial component and support previous identification of a highly fractionated iron impactor in glaciofluvial sand. Our results illustrate the possibility to study impact structures hidden beneath a thick ice sheet based on transported samples and this opens a new avenue for identifying other potential impact craters in Greenland and Antarctica.

INTRODUCTION AND BACKGROUND

The Hiawatha structure, located in Inglefield Land, northwestern Greenland is 31 km wide and was first described by Kjær et al. (2018). The structure has a rim-to-floor depth of 320 ± 70 m and is covered by the Greenland Ice Sheet, with ice thickness up to ~ 930 m (Figure 1; Kjær et al., 2018). The structure was initially proposed as a hypervelocity impact crater based on (i) its circular crater-like morphology with a muted central uplift imaged via airborne radar surveys, (ii) field observations of tangentially striking brittle structures adjacent to the curved bedrock rim in front of the ice margin, and (iii) shocked quartz grains with PDFs and individual glassy grains likely derived from shock-melted minerals within glaciofluvial sand collected in front of the structure and interpreted to be impact-related.

Modeling of subglacial drainage channels around the structure indicates local transportation of material out of the structure through a main drainage channel on its
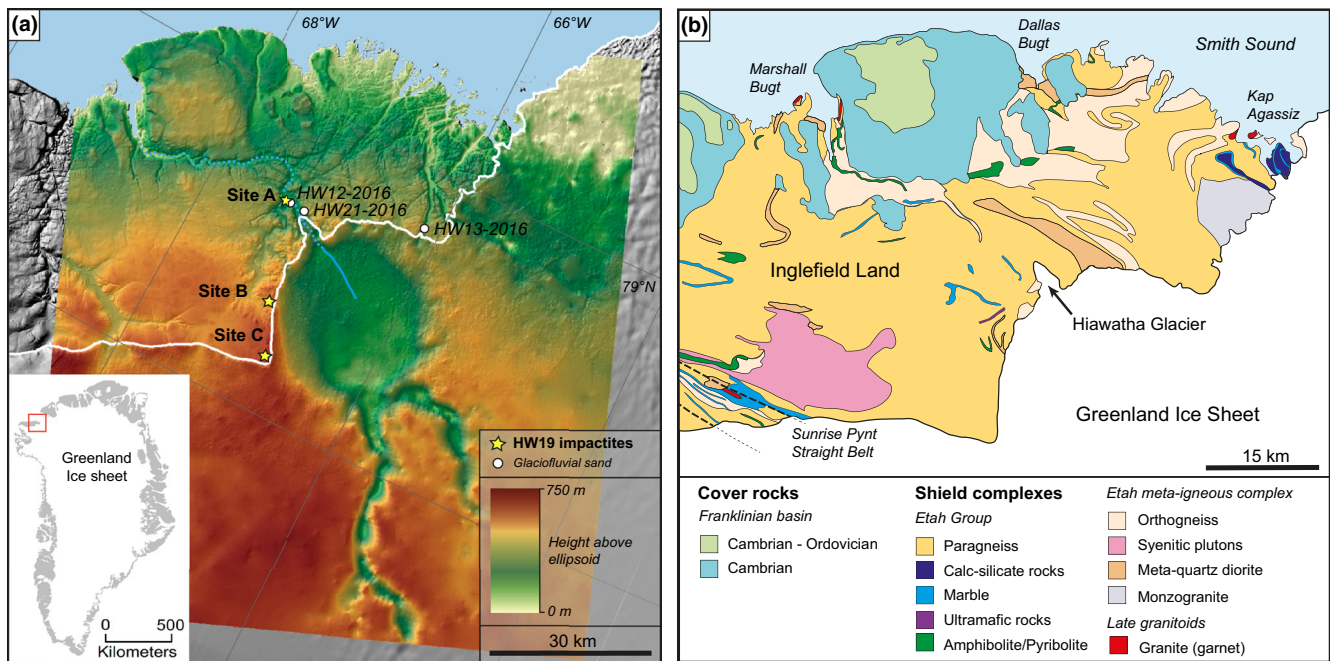
FIGURE 1. (a) Bedrock topography of the Hiawatha impact structure and surroundings. Current location of ice margin (white line) from Kjær et al. (2018). Inset map shows location of the Hiawatha impact structure in Northwest Greenland. Main subglacial drainage channel (blue solid line) and its continuation in the foreland (dotted line) show likely transportation pathway of the studied samples. Locations of HW19 samples and glaciofluvial sand (Kjær et al., 2018) shown by icons given in key. Sample locations: A—78.8417N-67.2941°E, B—78.6671N-66.9799°E, C—78.5892N-66.8157°E. (b) Geological map of the foreland, Inglefield Land, simplified from Dawes (2004) and Nutman et al. (2008).

northwestern side, running beneath the terminus of the narrow Hiawatha Glacier, an outlet glacier protruding from the Greenland Ice Sheet (Figure 1a; Bessette et al., 2021; Kjær et al., 2018). Three glaciofluvial sand samples (HW12-2016, HW13-2016 and HW21-2016) were collected from the foreland adjacent to the Hiawatha structure in 2016 (Kjær et al., 2018); the first two were collected 4 km downstream from the terminus of Hiawatha Glacier and the latter at the tip of the glacier (Figure 1). Comprehensive petrological and geochemical analysis of selected sand-sized grains from sample HW21-2016 revealed a variety of rapidly cooled, high-temperature melt grains with microporphyritic and microcrystalline textures and phase assemblages corresponding to typical products of a shock-melted peraluminous rock, interpreted to originate from eroded impact lithologies situated within the Hiawatha structure (Garde et al., 2022).

Recent U–Pb geochronology of shock-metamorphosed zircon grains from two glaciofluvial impact melt rocks (HW19-01 and HW19-05) collected from the foreland (Figure 1a), supported by Ar-Ar geochronology of selected sand-sized glaciofluvial melt grains (HW21-2016), yield a Late Paleocene impact age of 57.99 ± 0.54 Ma (Kenny et al., 2022). All this material is proposed to originate from the structure and therefore further underpin a hypervelocity impact event as the origin of the Hiawatha structure

(Kenny et al., 2022). Zircon grains seemingly unaffected by shock metamorphism within the two analyzed glaciofluvial melt rock samples reveal U–Pb ages that correspond to ages of local Proterozoic orthogneiss intrusions immediately adjacent to the structure, indicating local provenance of the two melt rock samples (Kenny et al., 2022). Although, of course, it is possible that some of the impact-related material derives from an unknown impact structure hidden under the ice, the only likely scenario is that it originates from the nearby Hiawatha structure. We follow the recommendation of Osinski et al. (2022): "samples in which shock metamorphic criteria are determined need not be in situ, as long as there is a clear topographic crater form and evidence (e.g., glacial flow directions) to connect the two". Clear evidence connecting sampled material to the Hiawatha structure under the ice has already been demonstrated (Figure 1a) (Kenny et al., 2022; Kjær et al., 2018), and here, we therefore refer to the crater as the Hiawatha impact structure herein. Previous studies have made use of float samples which have enabled valuable investigation of terrestrial impact craters, for example, Grieve et al. (1991) and Schmieder and Jourdan (2013). As direct sampling of the ice-covered Hiawatha impact structure is not possible without drilling, here we study rock-sized, glaciofluvial impact melt samples collected from the exposed foreland in front of the ice

margin of the Hiawatha Glacier and along the crater rim (Figure 1a).

REGIONAL GEOLOGY

The Hiawatha impact structure is situated in the lithologically diverse Inglefield Land, part of the Palaeoproterozoic Ellesmere–Inglefield mobile belt (Figure 1b) (Dawes, 2004, 2009; Dawes et al., 2000; Nutman et al., 2008). The exposed foreland immediately adjacent to the crater is dominated by the Palaeoproterozoic Etah Group (supracrustal migmatitic paragneisses), representing the oldest rocks in Inglefield Land with metamorphic U–Pb zircon ages of ~1930–1920 Ma (Nutman et al., 2008). Key components of the granulite-grade metasedimentary succession are felsic paragneisses with rock-forming garnet + sillimanite ± cordierite assemblages, marble and calc–silicate rocks, rare quartzites, and associated minor mafic–ultramafic rocks (Nutman et al., 2008). Marble and calc–silicate rocks within the supracrustal package are intercalated units with thicknesses ranging from minor meter-scale outcrops to ~2 km-wide units, as seen in the large east–west trending Sunrise Pynt Straight Belt extending from Sunrise Pynt to the glacial margin to the south of the Hiawatha impact structure (Figure 1b; Dawes et al., 2000; Nutman et al., 2008). These rocks contain both calcite and dolomite, as well as assemblages of silicate minerals including diopside, forsterite, spinel and wollastonite (Dawes et al., 2000).

The Etah Group is intruded by the marginally younger Palaeoproterozoic Etah meta-igneous complex (Dawes, 2004; Nutman et al., 2008). Units of this high-grade polyphase plutonic complex are seen in the vicinity of the Hiawatha impact structure (Figure 1b). Granitoid bodies ~1714 ± 15 Ma in age cutting gneissic fabrics of the paragneisses occur throughout Inglefield Land (Nutman et al., 2008). Younger Cambrian–Ordovician shelf carbonates dominate the coast of Inglefield Land in front of the Hiawatha Glacier around Dallas and Marshall Bugt (Figure 1b) and are part of the extensive Franklinian basin (Dawes et al., 2000; Ineson & Peel, 1987).

METHODOLOGY

Samples

Rock samples presented here were collected in 2019 from Inglefield Land at three locations (A–C) proximal to the Hiawatha impact structure (Figure 1a). Samples range from small pebbles to 1–2 kg boulders (Figure 2) and were selected in the field based on textures and clast contents that resembled impactite samples from other known craters. Samples from location A were collected ~4 km downstream from the terminus of the Hiawatha Glacier, from a wide riverbank on an active floodplain draining the Hiawatha impact structure through a main basal drainage path. These samples are proximal to glaciofluvial sand samples collected in 2016 (Garde et al., 2020, 2022; Gustafsson, 2020; Kjær et al., 2018). Samples HW19-01 and HW19-05, first described by Kenny et al. (2022), were both collected here. Sample localities B and C are located on topographic highs along the western flank of the crater rim and glacial margin (Figure 1a). All the samples show exterior rounding due to glaciofluvial transport.

Laboratory Analyses

Automated quantitative mineralogy (AQM) at submicrometer resolution and accompanying scanning electron microscope backscattered electron (BSE) imaging were performed at the Geological Survey of Denmark and Greenland, Denmark, following equipment, setup, and analytical procedures detailed in Keulen et al. (2020). Thin sections were studied with a ZEISS SIGMA 300VP Scanning Electron Microscope equipped with two Bruker Xflash 6|30 energy-dispersive spectroscopy (EDS) detectors with 129 eV energy resolution. Samples were analyzed with 12 kV, which reduces the interaction volume of the beam to approximately 500 nm (see Graham and Keulen, 2019 and Garde et al., 2022 for an in-depth description of this method). The EDS analyses are semiquantitative (standardless), include analyses for oxygen, and are normalized to 100%.

Electron microprobe (EMP) analysis was carried out at the University of Copenhagen. Wavelength-dispersive spectrometry (WDS) analyses were performed on a JEOL JXA-8200 Superprobe. Lithic clasts and crystalline matrix components were analyzed using a standard silicate setup where the spot size was set at 5 μm with a beam current of 15 nA and an accelerating voltage of 15 kV. Counting times were 20 s on peaks and backgrounds. The beam spot size was reduced to 2 μm for the analysis of individual microlite phases. Glasses were analyzed in a reduced energy mode to minimize the volatilization of the material, applying a 5–10 μm spot size and 5 nA beam current. The matrix correction used was p-φ-(ρz). Elements analyzed were SiO_2, Al_2O_3, TiO_2, FeO, MgO, CaO, K_2O, Na_2O, and FeO, while NiO, Cr_2O_3, and MnO were included in about half of the analyses only. Standards used were in-house silicate and oxide standards (see Garde et al., 2022). During the glass session, analyses were also made of selected standard glasses (ATHO-G and KL2-G) from Jochum et al. (2006). The analytical data were not recalculated to 100 wt% totals as alteration and hydrous phases are common. All EMP analysis data used in
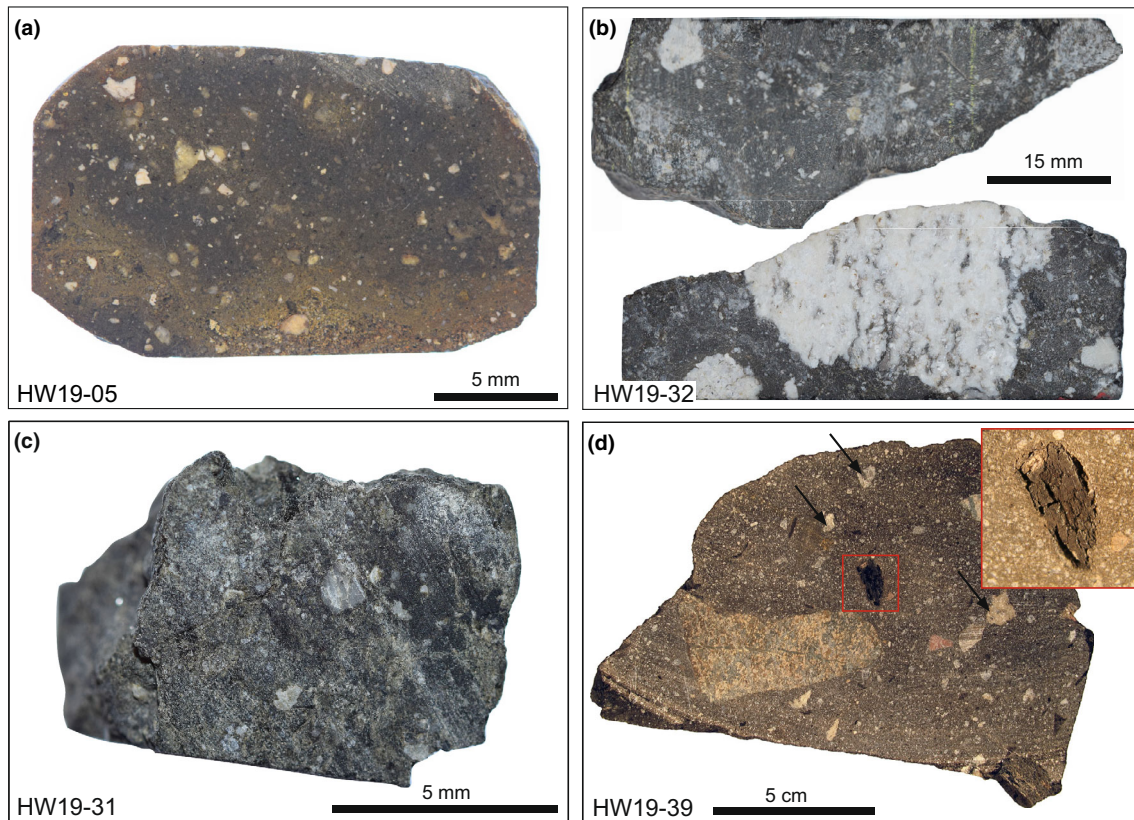
FIGURE 2. Melt rock hand specimens. (a) Cut surface of aphanitic, hypocrystalline clast-rich melt rock (HW19-05) with color variations in the matrix and clast ordering. From Kenny et al. (2022). (b) Two pieces of melt rock HW19-32 displaying a dark vitreous glass groundmass, partially melted polycrystalline fragments up to 20 mm across and smaller mineral fragments. (c) Clast-rich glassy melt rock with dark groundmass (HW19-31). (d) Melt rock sample HW19-39, characterized by an aphanitic, gray, carbonate groundmass and containing siliceous glass fragments (black arrows) and large granitic clasts. Inset image shows centimeter-sized organic fragment of charred wood.

this study and analyses of glass unknowns are given in Table S1.

Orientations of quartz PDFs were measured using a Leitz 5-axis universal stage mounted on a petrographic microscope at the American Museum of Natural History, United States. PDFs were measured from a selection of melt rocks where PDFs are common. Shocked grains that exhibit PDFs with between two and four sets of orientations per grain were measured. A total of 27 quartz grains from eight samples were measured, yielding 74 indexed planes. Four percent of the PDFs were unindexable. The measurements were indexed manually using projected stereonets, with 5 degree error ellipses, following French (1998) and Stoffler and Langenhorst (1994).

Five melt rock samples were analyzed for platinum group elements (PGE) and Au using NiS fire assay and Te co-precipitation followed by ICP-MS as outlined in McDonald and Viljoen (2006) at Cardiff University, United Kingdom. Melt rock samples were selected to represent different impact melt rock groupings based on

contrasting matrix textures and chemistry (Table 1). Rock chips (10–15 g) of each sample were cut to avoid weathered surfaces and large clasts, and then crushed and homogenized using an Mn steel jaw crusher and an agate ball mill. The resulting powder has a particle size of <125 mm and comprises a mix of matrix and lithic clasts. The rock powder was then split into two aliquots to perform duplicate analyses of each sample. Due to the presence of variable amounts of organic matter, a low-temperature ignition step was carried out at 500°C on all samples to avoid the formation of carbon globules, sulfide button disaggregation, and losses of PGEs as carbonyls from the NiS fire assay (De Vos et al., 2002; Juvonen et al., 2002; McDonald, 1993). All analyzed data and standards used are given in Table S2.

RESULTS

Twelve melt rock samples presented here were collected from the glaciofluvial floodplain in front of the

TABLE 1. Detailed petrographical descriptions of 12 glaciofluvial impact melt rock samples collected proximal to the Hiawatha impact structure.

Sample number	Location (site)	Classification (group)	Quartz (PDFs)	Zircon (shocked)	Description
HW19-01	A	Clast-rich impact melt rock (hypocrystalline)	Y	Y	Hypocrystalline feldspathic matrix with dispersed altered cordierite, biotite, and ilmenite microlites. Weak flow structures are seen throughout the groundmass. Shocked quartz fragments are often toasted and are partially digested in the matrix with mantles of biotite and SiO_2 and K-feldspar mesostasis. Checkerboard plagioclase, zircon, and monazite are common
HW19-02	A	Clast-rich impact melt rock (hypocrystalline)	Y	Y	Hypocrystalline melt rock matrix displaying microlite flow alignment and alteration. Needle-like amphibole and chlorite sit in place of orthopyroxene. Smectite crystallization is seen in areas of higher clast density. Common clasts include checkerboard plagioclase, shocked quartz, perthite–mesoperthite feldspars, garnet, sillimanite, kink-banded biotite as well as accessory monazite, apatite, ilmenite, and both shocked and apparently unshocked zircon
HW19-03	A	Clast-rich impact melt rock (hypocrystalline)	Y	Y	Hypocrystalline feldspathic microlite matrix with dispersed orthopyroxene and euhedral cordierite microlites. Sample shows minor alteration. The clasts are similar to HW19-01, with additional abundant mosaic quartz
HW19-04	A	Clast-rich impact melt rock (hypocrystalline)	Y	Y	Hypocrystalline feldspathic matrix with dispersed orthopyroxene, cordierite, biotite, and ilmenite microlites. Sample shows little alteration and is most well preserved of the hypocrystalline melt rocks. Shocked quartz and checkerboard plagioclase clasts common. Quartz grains surrounded by reaction corona of microlite-free mesostasis. Rare, decomposed feldspar fragments (now glass) with vesicles containing SiO_2 and K-feldspar mesostasis
HW19-05	A	Clast-rich impact melt rock (hypocrystalline)	Y	Y	Hypocrystalline feldspathic matrix containing shocked felsic clasts and high degrees hydrothermal alteration
HW19-06	A	Clast-rich impact melt rock (hypocrystalline)	Y	Y	Intensely hydrothermally altered, microlite-poor, melt rock matrix. Matrix is feldspathic in composition with widespread smectite replacement. Fine-grained quartz aggregates, garnet and feldspar clasts with perthite and mesoperthite intergrowths common
HW19-23	C	Clast-rich impact melt rock (hypocrystalline)	Y	Not seen	Hydrothermally altered and oxidized impact melt rock. Matrix supported, with dark aphanitic, Fe-rich matrix. Matrix is no longer microlitic. Sample is rich in microbrecciated clasts of quartz displaying PDFs and toasting, feldspars, and polycrystalline granitic aggregates
HW19-26	C	Clast-rich impact melt rock (hypocrystalline)	Y	Y	Hydrothermally altered clast-rich impact melt rock, with microlite-free feldspathic matrix. Former microlitic matrix has been replaced by Fe-rich feldspathic and amphibole-rich groundmass. Shocked quartz and feldspar clasts are common, as well as rare monazite, zircon, ilmenite, and titanite
HW19-28	B	Clast-rich impact melt rock (carbonate)	Y	Not seen	Brecciated clasts dominated by quartz and felsic rock fragments in a carbonate-rich matrix with weak flow structures. Pure calcite boarders clasts. Carbonate hosted veins run throughout the sample. The rock has a significant organic component, with centimeter-sized thermally altered wood fragments

TABLE 1. *Continued.* Detailed petrographical descriptions of 12 glaciofluvial impact melt rock samples collected proximal to the Hiawatha impact structure.

Sample number	Location (site)	Classification (group)	Quartz (PDFs)	Zircon (shocked)	Description
HW19-31	B	Clast-rich impact melt rock (glassy)	Y	Y	Glassy melt rock with pervasive perlitic fracturing and common melted K-feldspar clasts. Zircon, apatite, monazite, and shocked quartz grains are seen throughout the sample. Hydrothermal alteration and smectite crystallization occurs within fractures. Amorphized, vesicular organic material sits in glass
HW19-32	B	Clast-rich impact melt rock (glassy)	Y	Y	Clast-rich glassy impact melt rock with abundant spherulite growth, mineral melts, and widespread matrix flow structures. Highly shocked and brecciated clasts including partially melted polycrystalline felsic clasts with internal flow structures, numerous toasted quartz grains with PDFs, glass fragments, and partially digested clasts
HW19-39	B	Clast-rich impact melt rock (carbonate)	Y	ZrO_2 rim	Melted carbonate matrix supported melt rock with flow structures. Large vesiculated, siliceous glass clasts with calcite infill. Centimeter-sized organic fragments with well-preserved cell structures are common. Quartz PDFs are rare. Zircon grains are not granular, but ZrO_2 rims are seen

Note: Classifications following Stöffler et al. (2018) and characteristics of quartz and zircon based on petrographic and BSE imaging, respectively. Sample site locations are displayed in Figure 1a.

terminus of the Hiawatha Glacier and along the crater rim, proximal to the Hiawatha impact structure (Figure 1a). The samples are described following the criteria and nomenclature of Stöffler et al. (2018). A detailed petrographical summary and sample locations of all individual melt rock samples are given in Table 1. Thirteen additional collected samples are tentatively classified as lithic impact breccias and shown in Figure S1 and described in Table S3, but not discussed further.

Petrography of Impact Melt Rocks

All samples are clast-rich melt rocks, typically containing ~25–60 vol% clasts, both single mineral fragments and polycrystalline fragments ranging from <10 μm to >1 cm (Figure 2). The degree of matrix crystallinity in the melt rocks is highly heterogeneous. The melt rock samples are subdivided into three categories based on their degree of crystallinity and/or mineralogy, although samples within each subdivision are not texturally or chemically uniform: (i) hypocrystalline melt rocks, (ii) glassy melt rocks, and (iii) carbonate-based melt rocks. Shocked quartz grains with PDFs are present in all impact melt rock samples (Table 1).

Hypocrystalline Melt Rocks

This group of clast-rich melt rocks (eight samples) is characterized by a dark gray-brown, aphanitic silicate matrix (Figures 2a and 3). Matrices are dominated by lath-like plagioclase microlites with common "swallow-tail" habits, surrounded by mesostasis, both siliceous and K-feldspar-like in composition (Figure 4). Matrix heterogeneity exists on a micrometer-scale within individual samples (Figure 3). Microlite species rich in Fe and/or Mg are dispersed evenly throughout the feldspathic matrix (Figures 3b,d and 4). These include subhedral Fe-Mg pyroxene (orthopyroxene), euhedral but pinnitized cordierite, ilmenite, and Fe-oxides. Some samples contain hydrous phases, in place of other microlite species. For example, samples HW19-03 and HW19-04 contain both cordierite and orthopyroxene (~10–15 vol% combined), whereas these phases are sparse, if present at all, in HW19-02, where instead needle-like Al-Mg-rich amphibole (~98 wt% totals) and/or chlorite (80 wt% totals) are observed (Figure 4a,f). In some samples, devitrification of interstitial glass and microlite phases to Si-Al-(Fe-Mg)-rich clay varieties (smectite) and Fe-oxyhydroxide is seen.

Single mineral fragments dominate the clast load (Figure 3). They include quartz, plagioclase, K-feldspar including mesoperthitic to perthitic alkali feldspars, biotite, sillimanite, and garnet. Clasts are generally <400 μm across. Accessory zircon, apatite, and monazite are also observed within the matrix. Quartz clasts commonly contain embayments and are surrounded by 10–50 μm wide coronas of radially arranged orthopyroxene crystals and microlite-free K-feldspar mesostasis (Figure 3e,f). In samples where the matrix contains more hydrous phases,
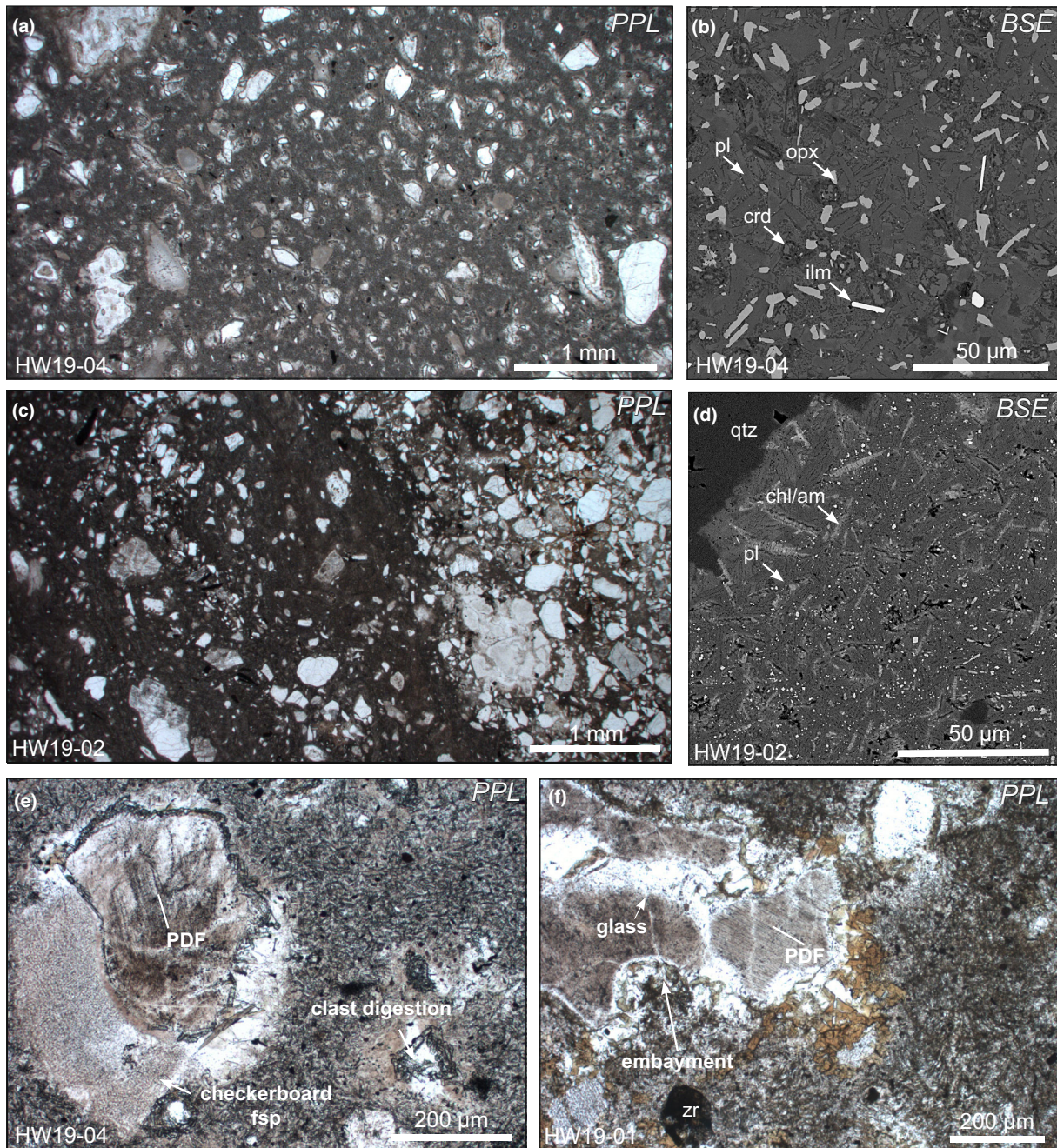
FIGURE 3. Photomicrographs and backscattered electron (BSE) images of hypocrystalline impact melt rocks. (a) and (c) Representative aphanitic microlitic matrix of two clast-rich melt rock samples. Evenly dispersed mineral fragments of felsic clasts seen in HW19-04, whereas HW19-02 shows uneven distribution of clasts and matrix flow structures. (b) and (d) Detailed images of hypocrystalline melt rock matrix, dominated by euhedral plagioclase microlites. New cordierite and orthopyroxene microlites occur in HW19-04, whereas HW19-02 contains needle-like microlites of chlorite and amphibole. (e) Shocked, strongly toasted quartz with PDFs adjacent to a checkerboard plagioclase in feldspathic matrix from HW19-04. Quartz clasts display coronas of orthopyroxene, and mesostasis surrounds grains. Smaller quartz clasts display variable reabsorption. (f) Shocked, toasted quartz with PDFs and embayments in sample HW19-01. Here, biotite in place of orthopyroxene surrounds quartz. Black grain (bottom left) is zircon which appears dark due to granular microstructure.

biotite + chlorite and smectite replace orthopyroxene and K-feldspar glass, respectively (Figure 3f). Clasts may display features of shock deformation or appear unshocked.

Shocked quartz clasts with decorated PDFs are common, with multiple sets of PDFs within single grains (Figure 3). Quartz grains with PDFs can exhibit strong toasting, that
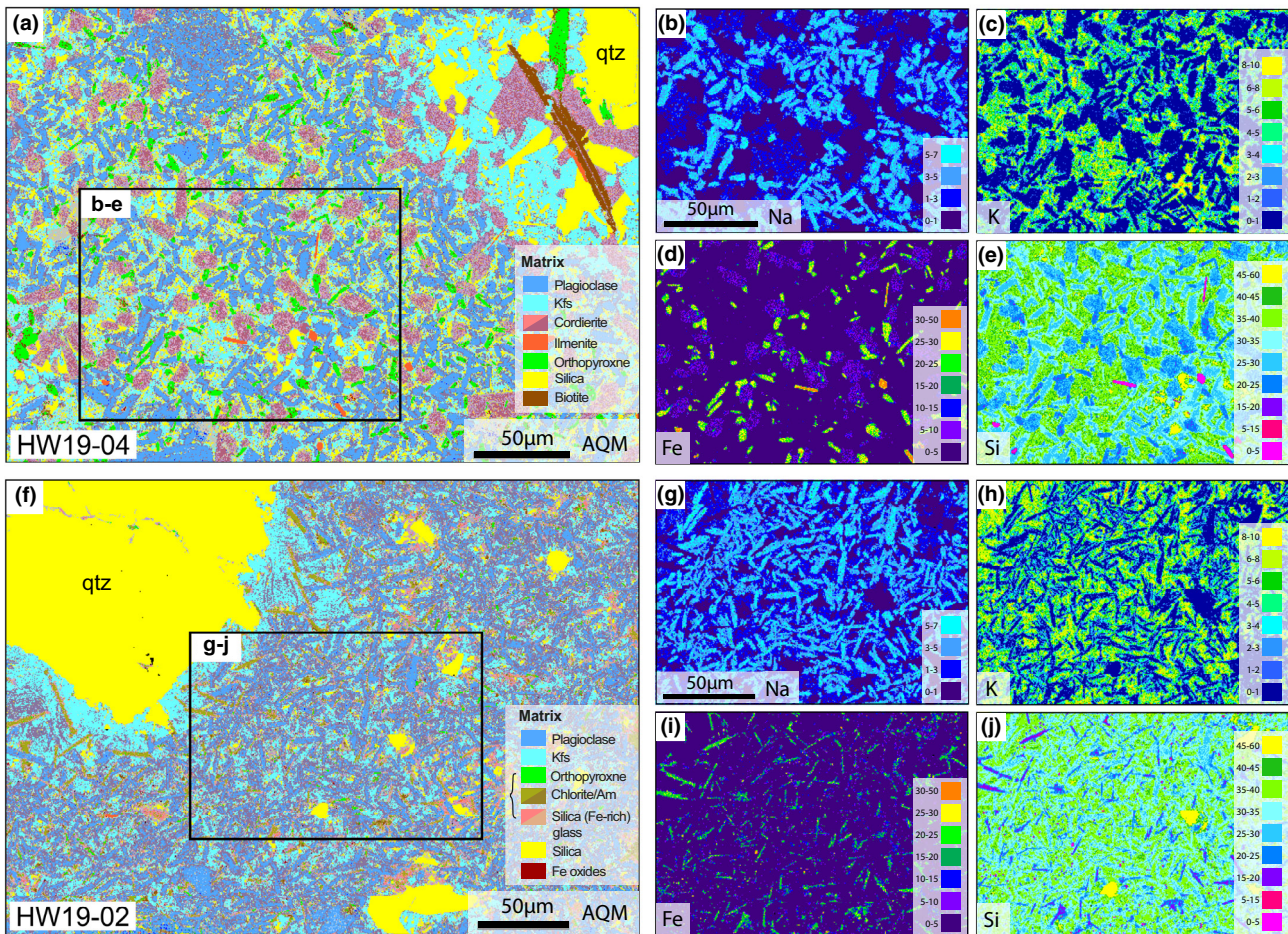
FIGURE 4. (a) and (f) Mineral-indexed AQM images of microlitic matrix from hypocrystalline impact melt rock samples HW19-04 and HW19-02, showing heterogeneity between samples. HW19-04 contains common dispersed cordierite and orthopyroxene throughout the matrix, whereas HW19-02 is cordierite-free and instead contains needle-like microlites with compositions corresponding to hydrous phases (e.g., chlorite and amphibole [Am]), Fe-rich silica glass, and small amounts of relict orthopyroxene (bracketed phases in key), indicating hydrothermal alteration and instability of the phases. Quartz clasts display partial resorption, surrounded by microlite-poor mesostasis (K-feldspar-like in composition). (b–e) and (g–j) Element composition AQM maps (wt%) in matrix with plagioclase microlites (Na: b and g), amorphous K-feldspar and silica mesostasis (K: c and h and Si: e and j), and Fe- (and Mg-) rich phases (Fe: d and i). BSE locations of (b–e) and (g–j) shown in Figure 3b,d.

is, display a brown, non-pleochroic appearance (cf., Whitehead, Spray, et al., 2002). Plagioclase feldspar clasts frequently exhibit a checkerboard texture (Figure 3e and Figure S2), with small rectangular subdomains of Na-rich feldspar surrounded by amorphous silica and K-feldspar glass (cf., Grieve, 1975). Rare brown fragments of glass with feldspar compositions contain numerous vesicles with internal rims of K-feldspar and centers of silica (Figure S3). Zircon grains within the melt matrix commonly display granular neoblastic and porous textures (cf., Timms et al., 2017), as well as micrometer-scale internal areas or external rims of ZrO_2 (Figure S4). In contrast, zircon grains situated in brecciated felsic clasts display either pristine or heavily metamict textures and these grains as such often show intact magmatic

growth zoning (Figure S4). Occurrences of shocked zircon within all samples are summarized in Table 1.

Glassy Melt Rocks

Two melt rock samples, HW19-31 and HW19-32, contain a microlite-free glassy groundmass and display high degrees of textural heterogeneity. Sample HW19-32 is dominated by a dark gray to black vitreous glass in hand sample (yellow in PPL; Figures 2b and 5a). Numerous densely packed spherulites are ubiquitous throughout the poorly mixed glass (Figure 5b). Spherulites exist as independent spherical growths or are seen to surround clasts and form elongate regions of devitrified glass within the matrix (Figure 5c). Central domains of plagioclase are found within some spherulites, surrounded by regions of
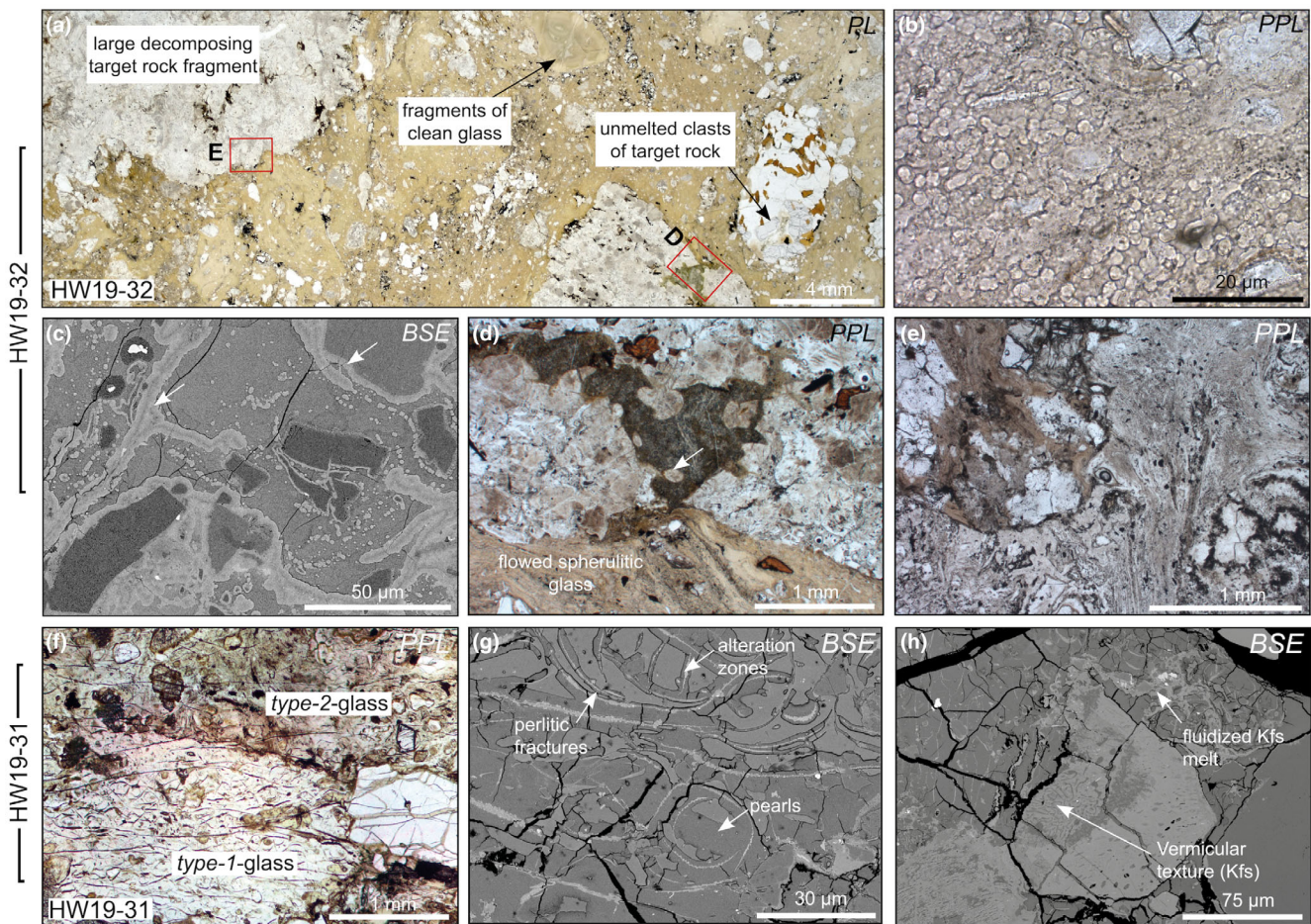
FIGURE 5. Images of glassy melt rocks. (a) Flow-textured, poorly mixed glassy groundmass of HW19-32. Polycrystalline clasts up to 3 cm across and fragments of clean glass are common. (b) Numerous, densely packed spherulites in glass groundmass. (c) Spherulites (light) in glass (dark). Elongate regions of devitrified spherulitic glass occur within bulk glass and surround lithic clasts. (d) Decomposing polycrystalline felsic fragment rich in toasted quartz with PDFs, with internal melt containing blebs of surviving quartz (arrow). (e) Mineral glasses with flow structures and vesicles within centimeter-sized felsic clast. (f) Sharp contact between type 1 (light and clast-poor) and type 2 (brown and clast-rich) perlitic glasses in sample HW19-31. Large, curvilinear fractures ($<200\,\mu m$) branch into smaller arcuate fractures $\sim50\,\mu m$ apart. (g) Perlitic fracturing and associated alteration zones within type 1 glass. Bright centers of hydrous alteration minerals are surrounded by smectite-filled fractures. (h) K-rich feldspar clast with vermicular texture, showing exsolution of plagioclase and quartz. Remobilization of K-rich feldspar controlled by pre-existing fracturing in the glass.

Mg-Fe-poor, Na-rich glass, and outer reverse zonation of K-feldspar mesostasis (Figure 6). The same zonation relationship is observed on the exterior of larger lithic fragments of plagioclase (Figure 6a).

Clasts within HW19-32 include single mineral fragments like those within the hypocrystalline melt rocks, including toasted quartz with decorated PDFs; however, centimeter-sized polycrystalline fragments are common here (Figures 2b and 5a). Many fragments are rich in toasted quartz and both diaplectic minerals and mineral glasses with flow structures following Stöffler (1984) (Figure 5e and Figure S5a,b). Small regions of surviving minerals exist within grains exhibiting internal decomposition (Figure 5d). Schlieric glass fragments with distorted vesicles are also

observed (Figure S5c). The intermingling of the mineral glasses is seen, which results in poorly mixed flow structures with differing compositions and new microspherulite growth $<2\,\mu m$ across (Figure S6). Zircon grains commonly display recrystallization and porous textures and rare plagioclase grains exhibit both inclined lamellae and alternate-twin deformation (Figure S5d; Jaret et al., 2014).

The second glassy melt rock, sample HW19-31, is characterized by a vitreous black glass matrix which is fractured and displays flow textures (Figure 5f). Two distinct, poorly mixed glass components are seen: Type 1 glass is relatively clast-poor and colorless, whereas type 2 glass is brown and relatively clast-rich. Both glasses are highly vesicular and contain pervasive perlitic fracturing
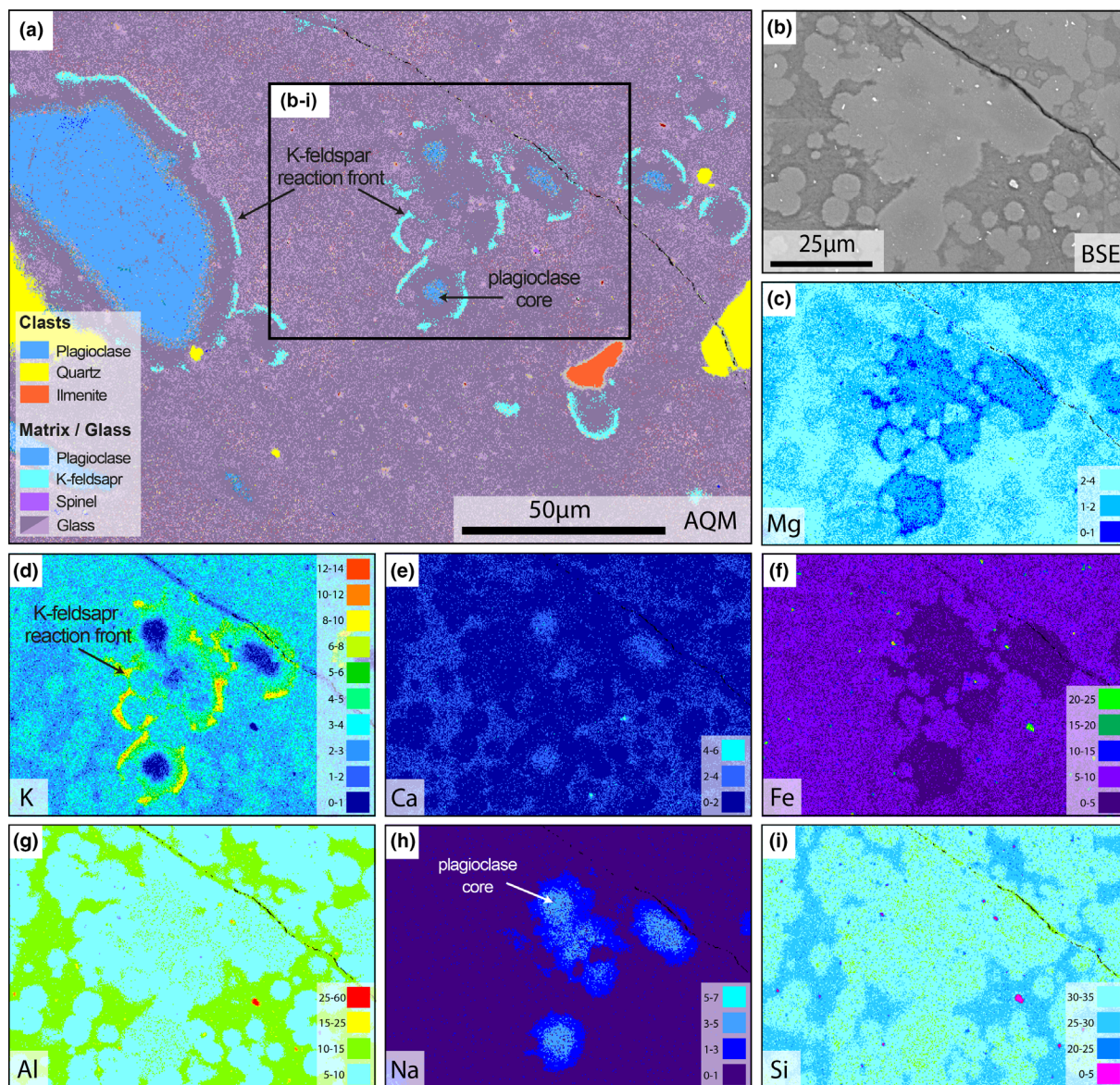
FIGURE 6. (a) Mineral-indexed AQM map of sample HW19-32. Bulk rock-forming glass (pink) with spherulites containing plagioclase cores and reverse reaction fronts of K-feldspar glass. Inset box displays area for images b–i. (b) BSE image of zoomed area, showing brighter spherulites in glass indicating higher atomic mass. (c–i) Element composition AQM maps (wt%) showing zoned spherulites.

throughout (Figure 5g). Perlitic fractures are filled with a hydrous Al-Fe-Mg-rich smectite mineral ($SiO_2 \sim 39$ wt%) with characteristic phyllosilicate cleavage. Smectite is also seen in place of entire areas of glass (Figure 7). Thin alteration zones of chlorite are observed in the center of smectite-filled fractures, which are often seen to extend further into the glass (Figure 7b). Clasts within HW19-31 are similar to those in the previously described melt rocks, although large polycrystalline fragments are absent (Table 1). In addition, ~ 1 mm K-feldspar clasts with vermicular textures and exsolution of quartz +

plagioclase sit within the glass (Figure 5h), in close association with densely packed K-feldspar spherulites within the smectite-replaced glass (Figure 7a).

Carbonate-Based Melt Rocks

Samples HW19-28 and HW19-39 comprise a clast-rich ($\sim 50\%$) small subgroup of samples characterized by a dark gray, aphanitic, carbonate groundmass (Figure 2d). Weak flow structures within the matrix and clast alignment are observed (Figure 8a). The matrix contains abundant finely brecciated silicate clasts, as well as large clasts with
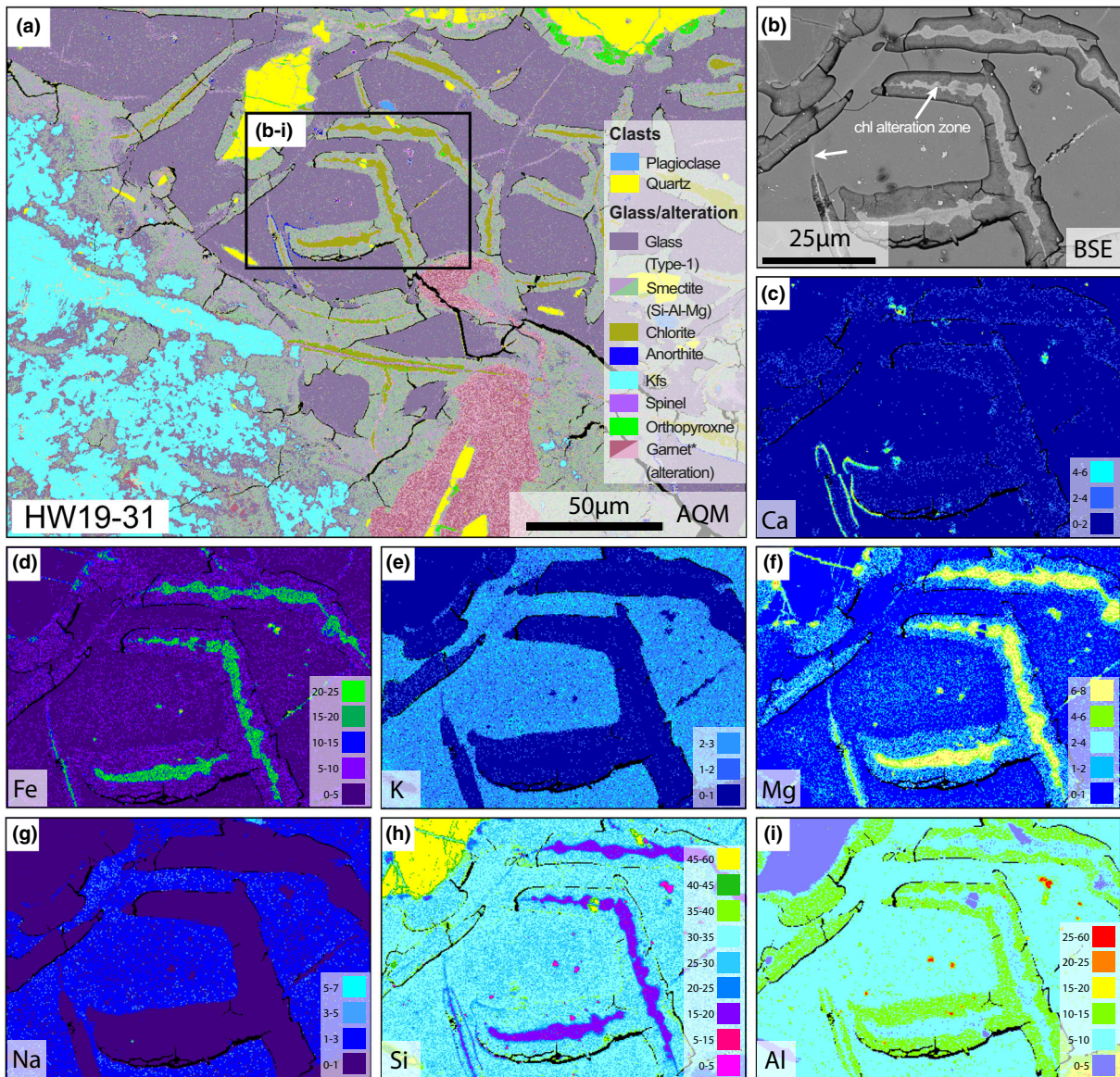
FIGURE 7. (a) Mineral-indexed AQM map of perlitic fracturing and hydrothermal alteration in type 1 glass from glassy melt rock sample HW19-31. Replacement of glass by smectite occurs along former perlitic fractures and in larger areas associated with K-feldspar. Centers of former perlitic fractures are lined by low-temperature alteration minerals including chlorite. Inset box shows location of images (b–i). (b) BSE image of perlitic fracture with smectite and chlorite alteration which is seen to extend past smectite-infilled fracture (arrow). (c–i) Element composition AQM maps (wt%) of glass replacement within former perlitic fractures. Images (c) and (i) display Fe-Mg-rich chlorite alteration.

overgrowths of clast-free, pure calcite (Figure 8b,c). Mg-rich (2–4 wt%) calcite dominates the matrix; however, chemical heterogeneity is observed, with trace amounts of Fe, Al, and Si throughout the calcite matrix (Figure 9).

Both samples contain brown-translucent, vesiculated glass fragments up to 2 cm in length (Figures 2d and 8d). The matrix of these glass fragments is siliceous; however, Al- and Si-free calcite fills the vesicles, forming crystalline globules within the glass up to 400 μm across (Figures 8d,e and 9). Fractures within the glass fragment connecting vesicles to the matrix show compositions alike the vesicle infill. Smaller crystalline pockets of calcite are also distributed throughout the matrix, but do not contain calcite globules (Figure 8f). Single mineral fragments of quartz and feldspar dominate the clast load (Figure 8a,b). In addition, large polycrystalline granitic rock fragments (<6 cm) are observed (Figure 2d). PDFs in quartz are observed rarely (Figure S7), whereas kink-banded biotite (Figure 8c) and planar fractures (PF) in quartz are common. Carbonate-filled embayments in quartz are also
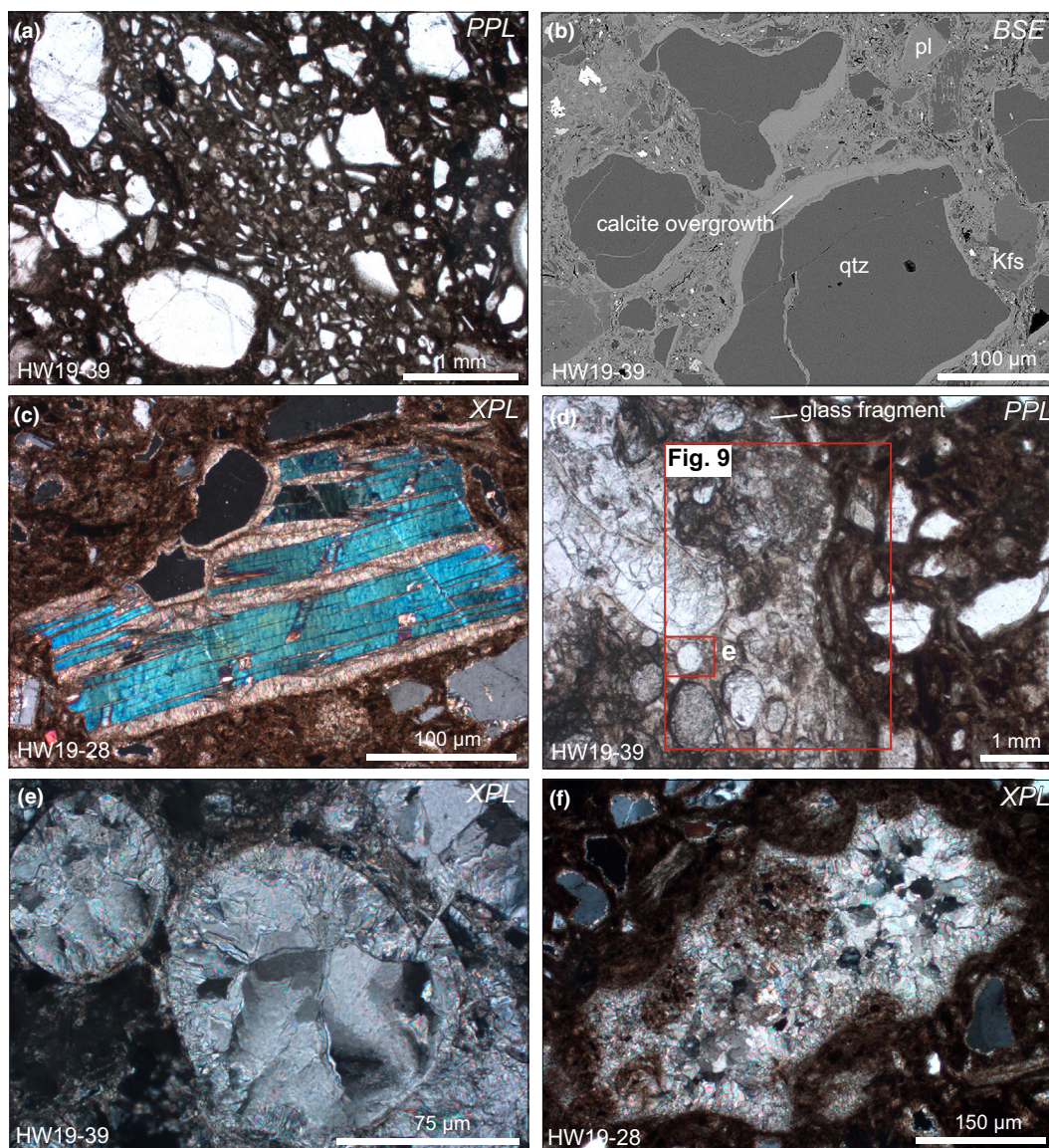
FIGURE 8. Imaging of carbonate-based melt rock samples. (a) Clast-rich sample HW19-39 with weak matrix flow structures and compositional variation. (b) Silicate clasts within carbonate matrix. Clast-free calcite mantles around lithic fragments. (c) Partially decomposed biotite fragment with open kinks filled with calcite. (d) Centimeter-sized silicate glass fragment (left) within dark, carbonate matrix. Circular structures (former vesicles) within glass fragment appear clear and generally lighter than matrix of glass fragment. Inset boxes show locations of image e and Figure 9. (e) Crystalline carbonate infilling of former vesicle in glass fragment, showing evidence of growth from wall to center. (f) Clast-free area filled with secondary crystalline calcite showing sharp contacts with the matrix and optically resembling that of the pure calcite coronas surrounding larger clasts.

found. Zircon grains within the carbonate samples appear apparently unshocked, although ZrO_2 rims are seen (Figure S4f).

Organic Material in Melt Rocks

Organic matter in varying proportions and states of preservation is observed within some melt rock samples. The organic matter was identified via petrography and inferred from EMP analysis and EDS spectra. The carbonate-based melt samples contain the greatest organic content, with centimeter-sized fragments of intact charcoal-like material and amorphized organic matter dispersed throughout the matrix (Figure 2d). These fragments display spectacular equidimensional box-shaped cell structures, which can be distorted, and cell structures are filled with carbonate-rich matrix (Figure 10a,b). Most of the silicate-based melts contain transformed organic material. HW19-31 contains vesiculated organic matter located between clasts and
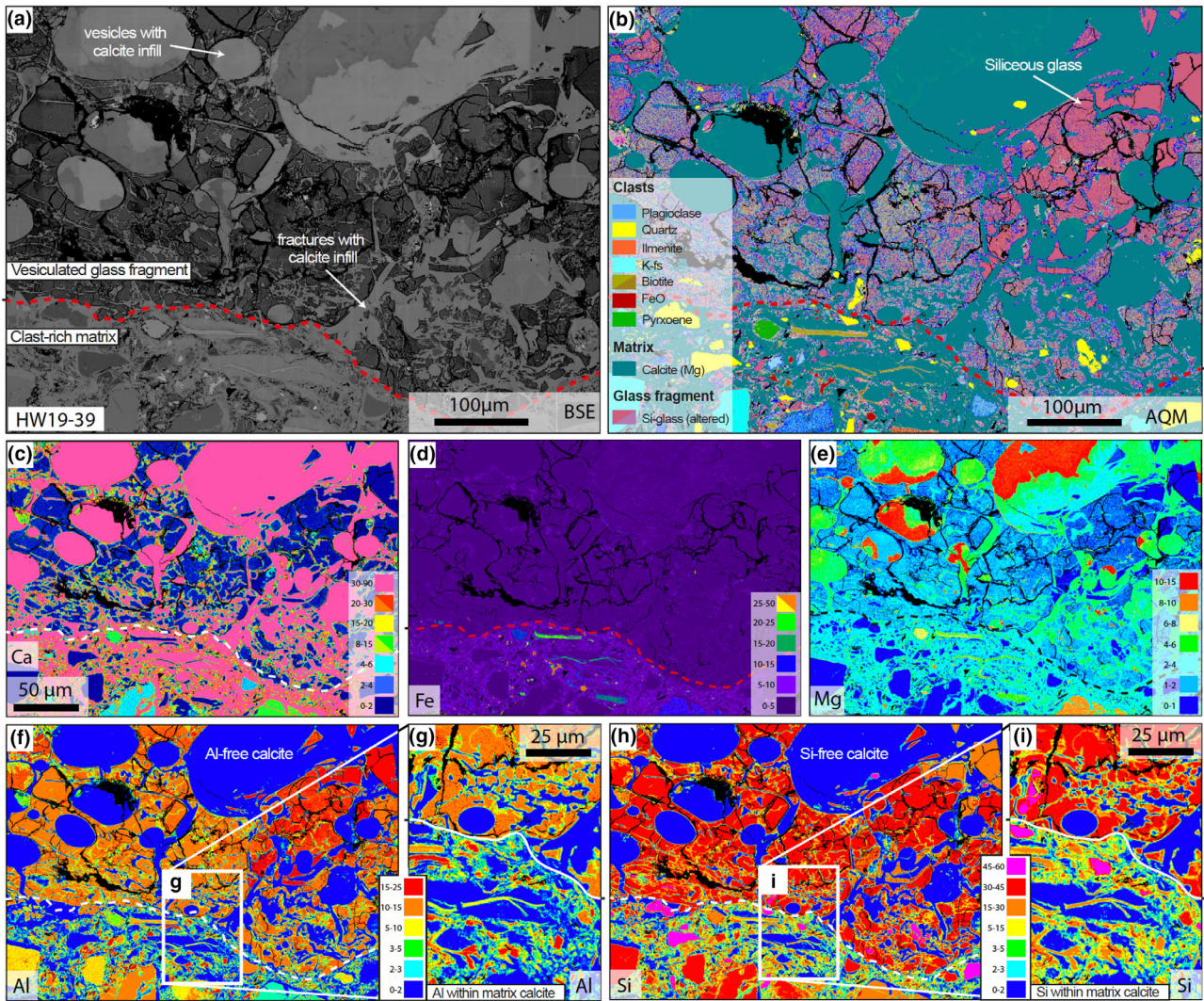
FIGURE 9. (a) BSE images of fractured, vesicular siliceous glass fragment within carbonate matrix from sample HW19-39. Dashed line denotes contact between fragment and matrix. Note filled fractures connecting carbonate-filled vesicles with carbonate matrix, indicating carbonate remobilization. (b) Mineral-indexed AQM map of same area. Vesicles within glass fragment are carbonate-filled and clast-free, except for minor quartz. Siliceous glass from fragment shows high degrees of chemical variation (with alteration). (c–i) Element composition AQM maps (wt%) of glass fragments and carbonate matrix. (c) Ca-rich nature of the matrix, vesicle infill, and connecting fractures. (d) Fe-poor calcite within glass fragment. (e) Peculiar lateral Mg zonation decreasing inward. Inset boxes in images (f) and (h) show area for images (g) and (i)—note elevation of Al and Si within matrix and the absence of such elements within the vesicle infill and connecting fractures (images g and i).

matrix components but displays no discernable cell structures (Figure 10c). Large vesicles within the glass of sample HW19-32 are filled with dark carbonaceous material (Figure 10d). Carbonaceous material is also found dispersed within the hypocrystalline melts, lining lithic fragments and microlites.

Quartz PDFs in Melt Rocks

Shocked quartz grains with characteristic PDFs are common in the hypocrystalline and glassy melt rocks. The orientations of quartz PDFs were measured in the melt rocks and the distribution of measured planes is displayed in Figure 11. Almost all PDFs are decorated by fluid inclusions and many grains are toasted. Grains containing two sets are the most common (12 grains), followed by four sets (eight grains), and least commonly three sets (seven grains). The most common PDF orientations are $\{10\bar{1}3\}$ and $\{10\bar{1}2\}$ (32% and 30% of observations, respectively). Twelve percent of plans occur at $\{10\bar{1}1\}$, with $\{11\bar{2}2\}$, $\{11\bar{2}1\}$, $\{21\bar{3}1\}$, $\{51\bar{6}1\}$, $\{10\bar{1}0\}$ and basal planes occurring at less than 7% (Figure 11e). The carbonate-based melt rocks contain far fewer shocked quartz grains (Figure S7).
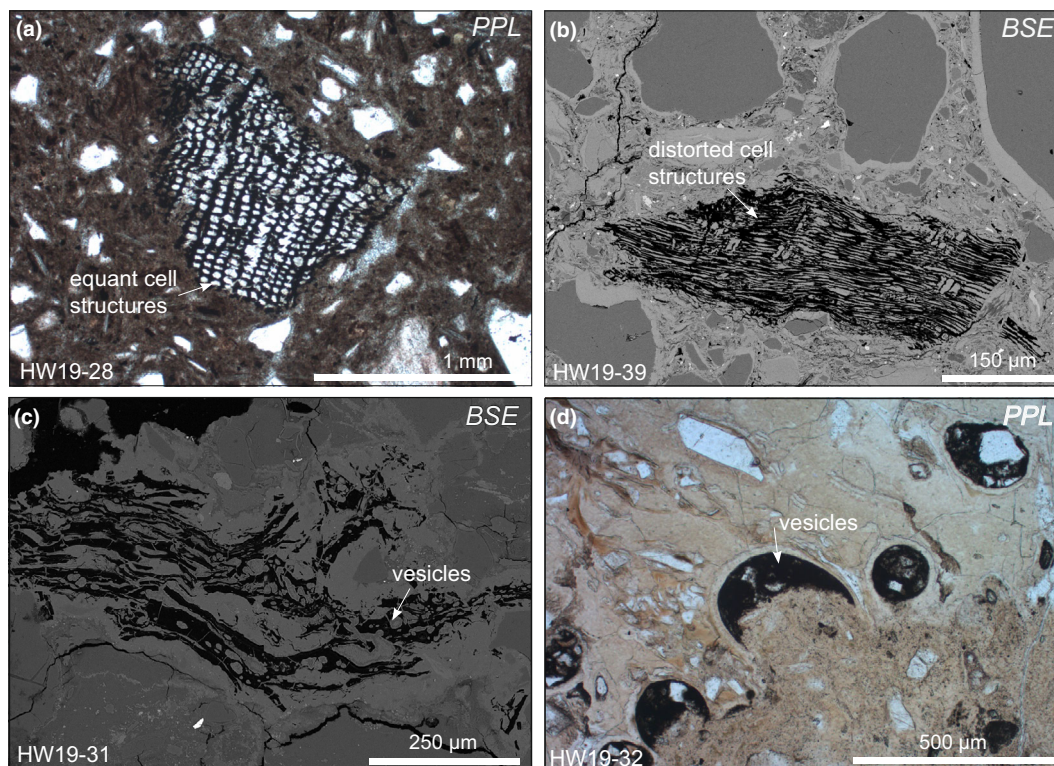
FIGURE 10. Photomicrographs (plane-polarized light, PPL) and BSE images of organic material within melt rocks. (a) Transverse cut of charred wood fragment preserving equidimensional, box-shaped cell structures filled with carbonate in carbonate sample HW19-28. (b) Tangential cut through wood fragment with distorted, carbonate-filled cell structures in carbonate sample HW19-39. (c) Vesicular organic material, amorphized within glass of sample HW19-31. (d) Vesicles infilled with carbonaceous material and lithic clasts in glassy sample HW19-32.

Chemistry of Impact Melt Rocks

Matrix/Melt Chemistry via EMP

Compositions of plagioclase microlites from hypocrystalline melt samples plot within the oligoclase–andesine fields (Figure 12) and have compositions of $An_{25-37}Ab_{57-66}Or_{4-12}$ (average: $An_{32}Ab_{60}Or_8$; Table 2). Sample HW19-03 shows a higher CaO composition at $\sim An_{49}Ab_{49}Or_1$. Interstitial K-feldspar mesostasis has compositions similar to K-feldspar glass bordering clasts and within embayments throughout all the hypocrystalline melt rocks (Figure 12b). Some feldspar compositions plot within the miscibility gap, between oligoclase–andesine and the K-feldspar mesostasis. Orthopyroxene microlites ($En_{41-57}Fs_{42-59}Wo_{<1}$) have compositions at the ferrosilite–enstatite boundary, and microlites located both within the matrix and in reaction coronas surrounding quartz clasts show high degrees of chemical consistency (Table S1).

All glasses analyzed from the two glassy samples show peraluminous compositions (Table 3). Sample HW19-32 shows high degrees of chemical heterogeneity between the bulk rock-forming glass, spherulites, and regions of flow-textured mineral glasses. The bulk rock-forming glass has low totals (~ 93.7 wt%) indicating a significant volatile component, and relatively low SiO_2 concentrations of ~ 51.8 wt%. Spherulites within the glass are chemically distinct from their host glass and compositions are feldspar-like. On average, the spherulites contain ~ 12 wt% higher SiO_2 than the glass and show higher wt% totals (~ 99 wt%). Poorly mixed, flow-textured mineral melts display compositions intermediate between the bulk glass and feldspathic compositions (Figure S5). The two individual perlitic glass components analyzed from sample HW19-31 show internally consistent compositions and have a significant volatile component (low EMP totals of 89–94 wt%), although the two glasses can be differentiated by discernable differences in all analyzed major element oxides except SiO_2 (~ 60 wt%) (Table 3). Type 1 glass shows K-Na-rich compositions, while type 2 glass is relatively Fe-Mg-rich.

Matrix analyses of carbonate-based melt rock sample HW19-39 show on average ~ 50 wt% CaO, ≤ 2 wt% SiO_2, significant MgO (2–9 wt%), FeO (2–4 wt%), and minor Al_2O_3 (~ 0.3 wt%; Table 3), corresponding to impure Mg-rich calcite. Unlike the silicate matrix in the other
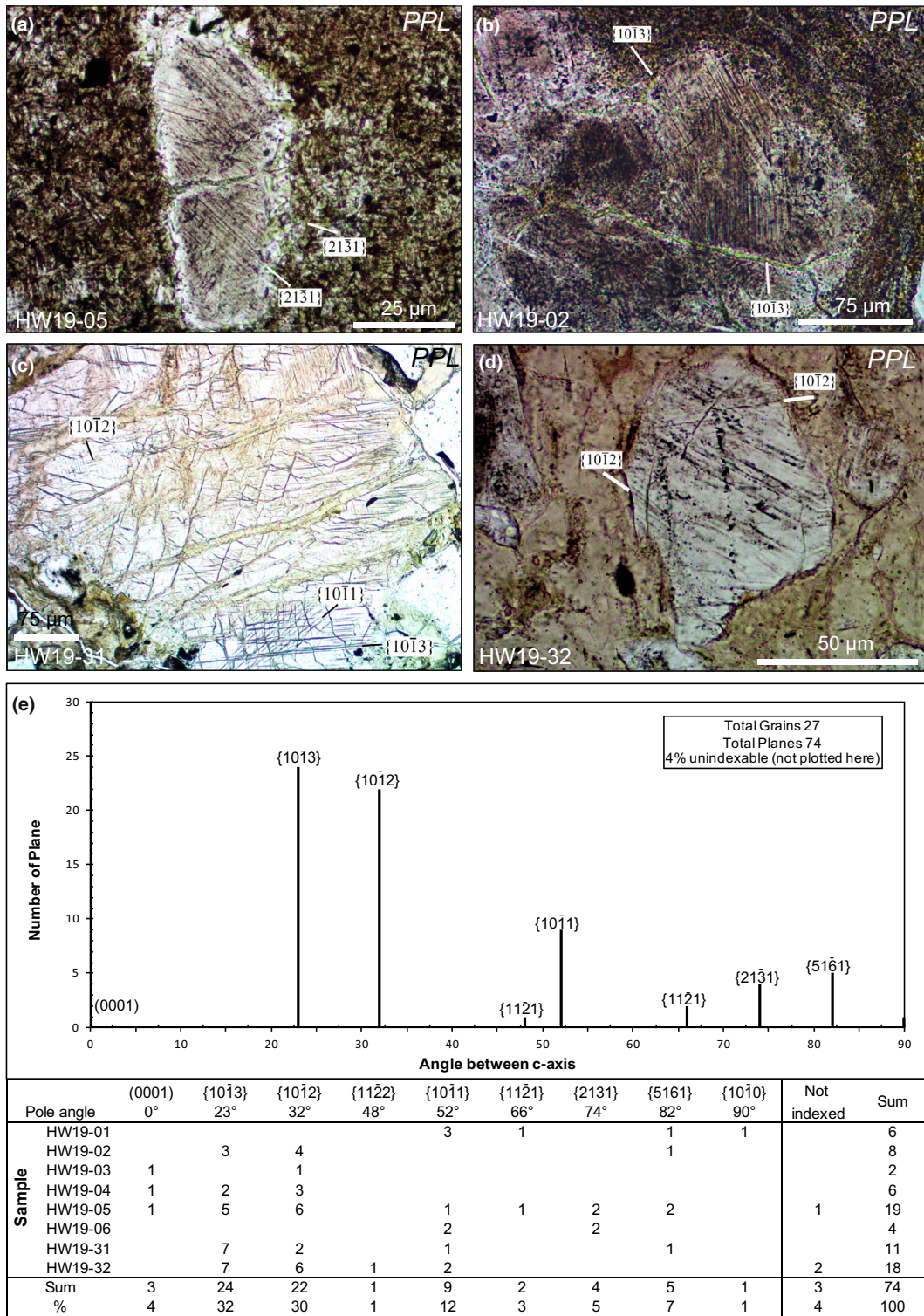
FIGURE 11. Shocked quartz grains with indexed PDFs from melt rocks (plane-polarized light, PPL). (a, b) Quartz grains from hypocrystalline melt rocks HW19-05 and HW19-02. (c, d) Quartz grains from glassy melt rocks HW19-31 and HW19-32. (e) Histogram and table of indexed PDF orientations (74 planes) from 27 grains.
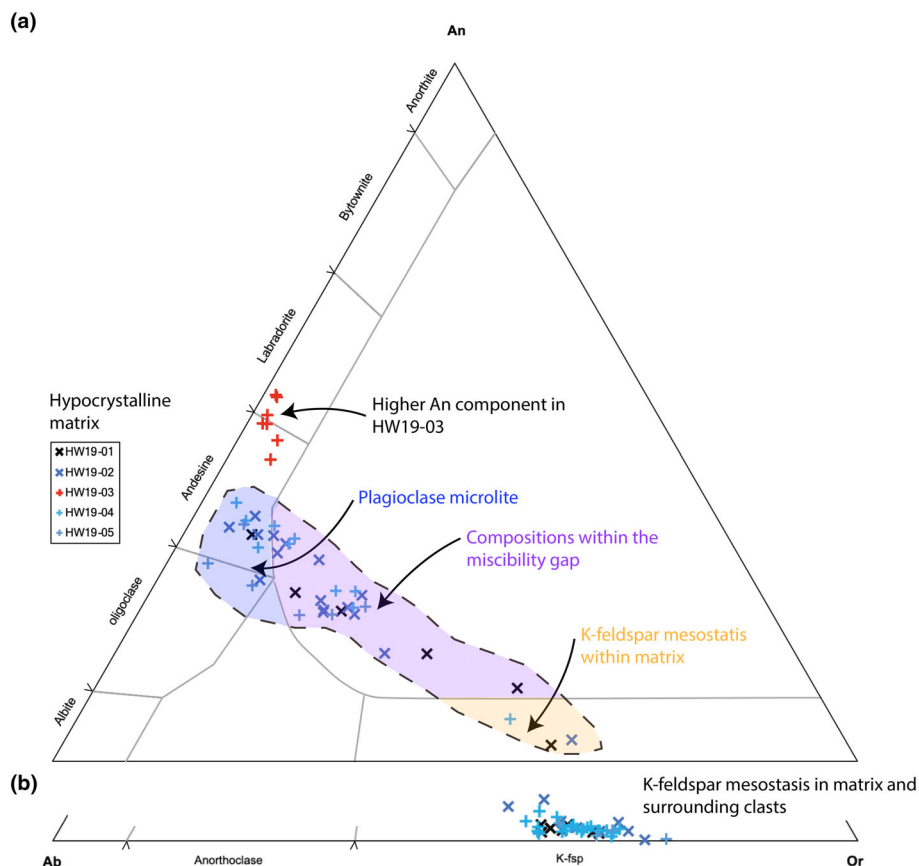
FIGURE 12. (a) Electron microprobe spot analyses of plagioclase microlites within the melt matrix of five hypocrystalline melt rocks. Analyses in the miscibility gap represent ternary feldspars or mixed analysis of various phases (K-feldspar and silica mesostasis). HW19-03 shows a higher Ca (anorthite) component when compared to the other samples. (b) Analyses of K-feldspar glass surrounding clasts and intestinal K-feldspar glass within microlitic matrix of the same samples.

TABLE 2. Average composition of plagioclase microlites from five hypocrystalline impact melt rocks.

| Sample number | HW19-01 | | HW19-02 | | HW19-03 | | HW19-04 | | HW19-05 | | Mean (excl. HW19-03) | |
| Number of analyses | 1 | | 4 | | 7 | | 3 | | 3 | | | |
	wt%	SD	wt%	SD	wt%	SD	wt%	SD	wt%	SD	wt%	SD
SiO_2	61.3	n.d.	62.9	3.4	56	1.8	60.7	2.1	62.3	2.2	62	3.8
K_2O	1.5	n.d.	1.4	0.5	0.5	0.3	1.2	0.4	1.3	0.5	1.3	0.5
Na_2O	6.7	n.d.	6.2	0.5	5.5	0.2	6.6	0.4	6.6	0.7	6.5	0.6
Al_2O_3	24.2	n.d.	22.9	1.9	27.5	1.2	24.1	1.6	21.8	1.6	23	2.8
FeO	0.2	n.d.	0.6	0.3	0.5	0.3	0.4	—	0.6	0.5	0.5	0.3
CaO	6.7	n.d.	6	1	9.9	0.9	7	1.0	5.5	1.0	6.2	2.1
MgO	—	n.d.	0.1	0.1	0.1	0.1	0.0	—	0.0	—	—	n.d.
TiO_2	0.1	n.d.	0.2	0.1	0.1	—	0.1	—	0.1	—	0.2	0.1
Total	101	n.d.	100	1	100	—	100	1	98	1	100	1.0
An	33		32		49		34		29		32	
Ab	59		60		49		59		63		60	
Or	9		9		3		7		8		8	

Abbreviations: An, anorthite; Ab, albite; n.d., not determined; Or, orthoclase; SD, standard deviation (2σ); wt%, mean composition in wt%.

two groupings, Al and Si are not contained in microlite phases but appear to sit within the calcite groundmass (Figure 9).

Platinum Group Elements

PGE abundances in five impact melt rock samples reveal two distinct groups (Figure 13 and Table 4). Three

TABLE 3. Average compositions of glass and carbonate groundmass from impact melt rocks.

Sample number	HW19-32						HW19-31				HW19-39	
Description	Bulk glass		Spherulites		Mineral melts		(type 1)		(type 2)		Calcite matrix	
Number of analyses	20		23		19		13		21		13	
	wt%	SD	wt%	SD	wt%	SD	wt%	SD	wt%	SD	wt%	SD
SiO_2	51.8	3.4	63.6	2.5	54.6	3.6	59.3	0.9	59.7	1.3	0.6	0.8
K_2O	3.3	0.7	3.7	1.5	3.9	0.8	3.4	0.4	0.5	0.2	—	n.d.
Na_2O	0.5	0.1	4.1	1.5	1.9	1.7	1.9	0.4	0.1	0.0	—	n.d.
Al_2O_3	20.6	1.7	17.2	0.6	20.1	1.8	16.1	0.3	18.9	0.5	0.3	0.4
FeO	9.2	1.5	5.2	1.3	6.4	2.1	4.7	0.3	7.2	0.5	3.5	0.8
CaO	2.6	0.5	2.4	0.8	5.8	1.6	1.3	0.1	1.8	0.1	49.6	3.7
MgO	4.9	0.6	2.4	0.5	3.1	1.0	1.8	0.2	3.6	0.3	4.1	1.8
TiO_2	0.8	0.1	0.7	0.1	1.3	0.4	0.5	0.1	0.3	0.2	—	n.d.
Total	93.7	2.7	99.4	2.7	98.1	1.9	89.2	1.1	92.2	1.8	58.4	1.0

Abbreviations: n.d., not determined; SD, standard deviation (2σ); wt%, mean composition in wt%.

silicate melt rock samples (HW19-01, HW19-31, and HW19-32) produce similar chondrite-normalized signatures that show elevated concentrations of Ir, Ru, Rh, and Pt relative to bulk upper continental crust (UCC). These samples display consistent chondrite-normalized positive Rh and negative Pt anomalies (($Rh/Ru)_N$ 2.4–4.2 and ($Pt/Rh)_N$ 0.6–0.9). Two carbonate-rich samples (HW19-28 and HW19-39) show UCC-like PGE abundances with a muted relative enrichment in Ru and Rh and subtle but consistent positive Rh anomalies (mean $(Rh/Ru)_N = 2.86$) without negative Pt anomalies (mean $(Pt/Rh)_N = 1.48$). Duplicate analyses of each sample show little deviation (Table S2).

DISCUSSION

Observations presented here provide the first comprehensive investigation of glaciofluvial impact melt rock samples collected from the ice margin in Inglefield Land (Figure 1a). With the only likely origin of the samples being from the Hiawatha impact structure, this work adds to previous studies of impact-related material collected in Inglefield Land and strongly supports the identification of a hypervelocity impact event (Garde et al., 2020, 2022; Gustafsson, 2020; Kenny et al., 2022; Kjær et al., 2018). All the studied samples are melt rocks and contain a variety of shocked, unshocked, and melted materials mixed during their formation. The melt rock samples display high degrees of variation, both in sample matrix (e.g., melt matrix textural and chemical heterogeneity) and shock metamorphism in minerals (see Results Section). This is typical of impact materials in both crater-fill deposits and in impact ejecta deposits (Mader & Osinski, 2018; Osinski et al., 2018), as seen in other impact structures, for example, El'gygytgyn, Russia (Gurov & Koeberl, 2004); Ries, Germany (Osinski, 2003; Stöffler et al., 2013); and Gardnos, Norway (French et al., 1997; Kalleson et al., 2010).

Impact Melt Rocks

Hypocrystalline and Glassy Melt Rocks

Aphanitic, hypocrystalline melt is a well-documented melt rock matrix texture in terrestrial impact craters (Dressler & Reimold, 2001). The presence of interstitial silica and K-feldspar glass within the matrix, paired with the small size of microlite phases, indicates fast cooling of the superheated melt upon formation (Figure 4). Common "swallowtail" terminations of plagioclase microlites (Figure 3b) and plagioclase microlite compositions plotting within the miscibility gap (Figure 12), which potentially represent ternary feldspars with unusual compositions (Osinski, 2004), suggests quenching at high temperature without full re-equilibration and rapid, diffusion-controlled growth (Lofgren, 1974; Osinski, 2003). However, subsequent cooling was slow enough to allow the widespread formation of orthopyroxene microlites in the matrix and in coronas surrounding quartz clasts, leading to the variable assimilation of clasts (Figure 3) (c.f., Whitehead, Grieve, et al., 2002), as observed, for example, in impact melt rocks from Mistastin (Grieve, 1975) and Sääksjärvi and Lappajärvi (Schmieder & Jourdan, 2013). In contrast, two samples contain a glassy, microlite-free matrix: Sample HW19-32 is comprised of multiple poorly mixed, flow-textured mineral glasses reflecting incomplete melt homogenization during mixing (Figure 5). Vesiculation and schlieren observed within the glass are characteristic of mineral glasses (Stöffler, 1984), indicating rapid cooling from high temperatures upon melt generation and a relatively short duration of the high-temperature excursion, resulting in low or inhibited nucleation of new matrix phases. Similarly, perlitic glasses type 1 and type 2 in sample HW19-31 are interpreted to represent different mineral glasses which
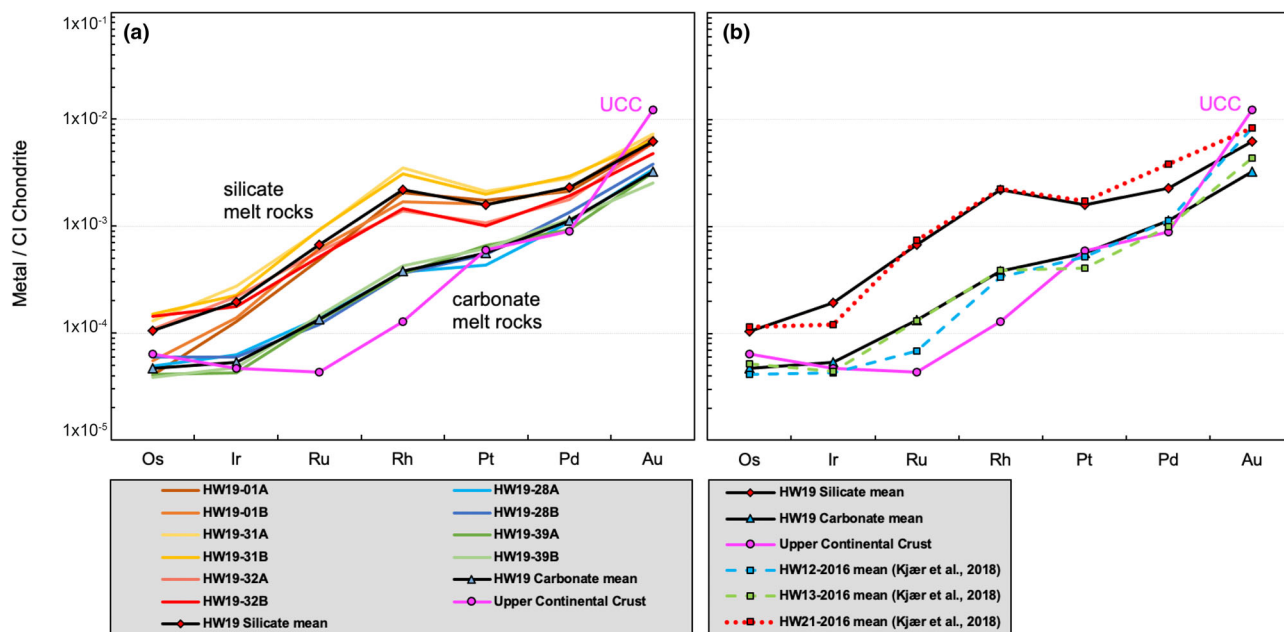
FIGURE 13. (a) CI-chondrite-normalized platinum group element patterns (PGE) and Au abundances for melt rocks compared to upper continental crust (UCC). Duplicate analyses of each sample show highly similar abundances (Table 4). A clear separation between the PGE-enriched silicate and PGE-poor carbonate-based samples is shown. Mean concentrations of both groups shown by black lines (b) Average CI-chondrite-normalized PGE abundances from the silicate melt rocks and carbonate-based melt rocks plotted against average values of three samples of sand from Kjær et al. (2018). HW21-2016 is rich in impactite grains, whereas samples HW12-2016 and HW13-2016 contained little or no impact-related material and are noted as being chemical analogs of local crust (Kjær et al., 2018). Values for chondrite normalization from Lodders (2003). UCC values (pink) from McLennan (1998) and Park et al. (2012).

were poorly homogenized in a semiplastic state and underwent subsequent rapid cooling (Figure 5). Both glasses show chemical distinction and likely originate from the melting of different crystalline mineral phases: Type 1 glass contains a feldspar-like composition, whereas type 2 is more likely to be the product of a mafic mineral melt (e.g., biotite), being relatively richer in Fe and Mg (Table 3).

The mixture of variably shocked mineral clasts and differing melt textures observed within the samples reflects a three key aspects of impact metamorphism: (a) the shock distribution itself is known to be heterogeneous (French, 1998; Sharp & DeCarli, 2006), (b) incorporation of material into these rock types is a highly energetic, and components of the resulting mixed material in a given sample need not have originated from the same location prior to impact, and (c) melting is controlled by a wide variety of characteristics including water and other volatile contents, and porosity of the target materials (Jaret et al., 2017; Kieffer & Simonds, 1980; Osinski, 2007; Osinski, Grieve, et al., 2008; Sharp & DeCarli, 2006). Additionally, the variable cooling rates observed within the samples can be readily explained by the prolonged cooling time of the crater to ambient conditions and the original position of the material within the crater, because cooling

rates vary both locally and across the structure (e.g., central uplift and within the breccia lens; Kenny et al., 2019; Schmieder & Jourdan, 2013). For these reasons, the exact shock conditions within each sample cannot be determined. However, the suggested P/T conditions for the formation of these melt samples are likely in the order of >2000–2500 K and pressures of >60 GPa for shock melting of dense, silicate rock (Grieve et al., 1997; Stöffler et al., 2018), allowing for the high P/T shock features observed within the samples.

Carbonate-Based Melt Rocks

In contrast to the melt matrices of the hypocrystalline and glassy siliceous melt rocks, the carbonate melts display a flow-textured calcitic groundmass ($\sim$50 wt% CaO; Table 3). Impact melting of carbonate rocks remains poorly understood compared to silicate rocks (Osinski, Spray, & Grieve, 2008; Stöffler et al., 2018). Significant Si and Al contents ($\leq$2 wt% SiO_2 and $\sim$0.3 wt% Al_2O_3) are found within the Mg-rich calcite matrix of sample HW19-39, and not limited to the numerous microclasts. Such element enrichment in calcite and dolomite has been used as evidence for an impact melt origin of carbonate-rich material in other impact craters (e.g., Osinski & Spray, 2001; Osinski et al., 2004; Walton

TABLE 4. Platinum group element (PGE) data for impact melt rocks.

Sample	Analysis	Os	Ir	Ru	Rh	Pt	Pd	Au	Analysis	(Pd/Ir)N	(Rh/Pt)N	(Ru/Rh)N
HW19-01	A	0.02	0.06	0.33	0.29	1.74	1.24	0.87	A	16.45	1.18	0.24
	B	0.03	0.07	0.42	0.24	1.60	1.31	0.99	B	16.05	1.06	0.36
	SD	0.005	0.004	0.065	0.036	0.099	0.051	0.084	Mean	16.25	1.12	0.30
HW19-31	A	0.06	0.13	0.63	0.49	2.12	1.64	1.06	A	10.13	1.66	0.26
	B	0.07	0.11	0.65	0.44	2.00	1.73	0.94	B	12.99	1.56	0.30
	SD	0.007	0.016	0.008	0.040	0.085	0.065	0.083	Mean	11.56	1.61	0.28
HW19-32	A	0.05	0.10	0.40	0.19	1.07	1.04	0.88	A	8.14	1.29	0.42
	B	0.07	0.08	0.35	0.20	1.00	1.12	0.70	B	10.80	1.45	0.35
	SD	0.012	0.014	0.032	0.007	0.051	0.057	0.127	Mean	9.47	1.37	0.39
HW19-28[a]	A	0.02	0.03	0.10	0.05	0.44	0.64	0.50	A	17.53	0.86	0.37
	B	0.03	0.03	0.08	0.05	0.54	0.79	0.56	B	22.45	0.67	0.33
	SD	0.004	0.001	0.009	0.002	0.075	0.101	0.041	Mean	19.99	0.76	0.35
HW19-39[a]	A	0.02	0.02	0.09	0.05	0.66	0.55	0.46	A	21.80	0.55	0.37
	B	0.02	0.02	0.10	0.06	0.62	0.68	0.37	B	24.19	0.69	0.34
	SD	0.001	0.002	0.006	0.006	0.031	0.095	0.064	Mean	22.99	0.62	0.35
Silicate melt rock	Mean	0.05	0.09	0.47	0.31	1.59	1.35	0.91	Mean	12.4	1.4	0.3
	SD	0.02	0.03	0.14	0.13	0.46	0.28	0.12	SD	3.3	0.2	0.1
Carbonate melt rock	Mean	0.02	0.02	0.09	0.05	0.57	0.66	0.47	Mean	21.5	0.7	0.4
	SD	0.005	0.004	0.008	0.004	0.087	0.102	0.077	SD	2.5	0.1	0.0

Note: All abundances given in ppb. Ratios are normalized using chondrite values from Lodders (2003).

Abbreviation: SD, standard deviation (2σ).

[a]Carbonate-based sample.

et al., 2019), because such high Al_2O_3 and SiO_2 contents in non-impact-related carbonates are otherwise only known from terrestrial carbonatites (Osinski et al., 2005). Areas of matrix in the carbonate samples here containing 5–10 wt% Al_2O_3 and 5–30 wt% SiO_2 (Figure 9) are likely postimpact hydrothermal clays and not true element enrichment in the calcite matrix. Flow textures, glass fragments and PDFs in quartz (Figure S7) indicate that sample HW19-39 was formed soon after the impact and was once mainly molten, and the aforementioned element enrichment in the calcite matrix is therefore interpreted as the incorporation of silicate material at high temperatures, likely by partial digestion of silicate clasts. However, according to Osinski et al. (2004), it is unclear if such Si and Al are incorporated into the calcite structure, or if quenching of the carbonate-rich melt leads to the crystallization of nanometer-sized silicate phases.

Recognition and classification of shock metamorphic stages in carbonates is much more complex than for silicates (Osinski, Spray, & Grieve, 2008). Furthermore, impacting into volatile-rich or porous rocks dramatically reduces cratering efficiency (Wünnemann et al., 2008). Partial dissociation textures in zircon (Figure S4) indicate high temperature in the carbonate-based melt breccias at Hiawatha, whereas shock indicators of high pressure are present, but rare (Figure S7). No evidence for calcite decomposition was observed in the samples here. Experimental studies have suggested pressures required for calcite decomposition ranging from as high as >65 GPa (Gupta et al., 2002) down to 10–20 GPa (for >10%–50% decomposition) (Lange & Ahrens, 1986). It is stated that temperature is the limiting factor, and that melting of calcite can occur at lower pressures than melting of dense, crystalline silicate rocks (Osinski, 2007). Therefore, we suggest that these samples represent melting of volatile-rich carbonate at high temperatures, but relatively low pressures when compared to the silicate melt rocks at the Hiawatha impact structure.

Target Sequence of the Hiawatha Impact Structure

The original locations of the individual impactite samples in relation to the crater are of course unknown. Given the ~58 Ma age of the impact, it can be ruled out that Hiawatha melt rocks were sampled from an ejecta blanket preserved until today under the ice (or that any of the ejecta blanket remains in the foreland). Previous studies have shown that impact-related material was transported subglacially from the Hiawatha impact structure through the main subglacial drainage channel to the adjacent floodplain (Figure 1a; Garde et al., 2022; Kenny et al., 2022; Kjær et al., 2018).

Silicate Impact Melt Rocks

The melt rocks studied here that are predominately composed of silicate melt and glass certainly originate from shock-melting of crystalline meta-sedimentary and meta-igneous lithologies, such as those which dominate

the exposed foreland of Inglefield Land. The Al_2O_3-rich glassy melts and coexisting matrix microlites of plagioclase + cordierite + orthopyroxene + biotite in the hypocrystalline samples are peraluminous in composition (Tables 2 and 3) and are typical crystallization products from a peraluminous melt (Clemens & Wall, 1988) matching the Etah Group paragneiss, supporting local provenance. Similar matrix textures and chemistry of the sand-sized glaciofluvial melt grains reported by Garde et al. (2022) were interpreted to have the same origin. The higher Ca content seen in plagioclase microlites from HW19-03 likely represents Ca variability in the target rock or mixing of different target rock components (Figure 12), although Ca-metasomatism during postimpact hydrothermal alteration could also explain this relative Ca enrichment. Dominant mineral clasts in the silicate melt rocks, summarized as quartz + plagioclase + K-feldspar + biotite ± sillimanite ± garnet (Table 1), mirror the metamorphic mineral assemblage of the Etah Group and Etah meta-igneous complex (Dawes, 2004; Nutman et al., 2008), as well as the predominant mineral species in the melt grain-rich glaciofluvial sand exhumed from the structure (Garde et al., 2022; Kjær et al., 2018). Furthermore, most U–Pb ages of apparently unshocked zircon from HW19-01 and HW19-05 (Kenny et al., 2022) correspond to known zircon ages found in Inglefield Land, proximal to the Hiawatha impact structure (Nutman et al., 2008).

Source Rock of Carbonate-Based Melt Rocks

The formation of carbonate-dominated impact melts requires a significant volume of carbonate rocks in the target area and therefore indicates a mixed target sequence for the Hiawatha impact structure. Carbonate-rich lithologies from the ice-free land adjacent of the Hiawatha impact structure include Etah Group marble and associated calc–silicate rocks, as well as Franklinian, Cambrian–Ordovician shelf carbonates exposed along the coast of Inglefield Land, which extend all along the coast of North Greenland (Dawes et al., 2000). In the ice-free part of Inglefield Land, the latter rocks only occur along the coast (Figure 1a), contrary to other parts of northern Greenland, for example, Daugaard-Jensen Land ~75 km to the northwest of Inglefield Land, where their coverage reaches inland (Dawes et al., 2000). Higgins et al. (1991) suggest that these carbonate platforms were more extensive in Inglefield Land during most of the Early Paleozoic and, therefore, it is possible that remnants of the platforms remained in the target area in the Late Paleocene and have since been removed by glacial erosion. However, other unknown carbonate-rich lithologies may also exist under the ice or have been present in the target area.

Hydrothermal Alteration

Hydrothermal alteration is often present in impact structures; however, the nature and timing of the interaction between impact material and fluids is highly variable (Osinski et al., 2013; Pirajno, 2005). We observe evidence of postimpact hydrothermal alteration and the interaction with contained water within the melt, in all the melt rock samples, for example, the replacement of dry microlite phases with hydrous phases (i.e., amphiboles and chlorite) and widespread devitrification of interstitial glass to smectite (Figure 4). Additionally, widespread devitrification of the glass in sample HW19-32, where glass is being replaced by small aggregates of acicular crystals forming numerous spherulites (Lofgren, 1971; McArthur et al., 1998; Figure 5), indicates supercooled, high viscosity melts (Kieth & Padden, 1963) where nucleation is controlled by impurities (i.e., finely brecciated microclasts, observed here with plagioclase cores (Figure 6), as well as contained water within the melt). Pervasive perlitic fracturing seen in sample HW19-31 (Figure 5f) is typical of hydrated glass and is observed in samples from other terrestrial impact craters (Garde et al., 2022; Grieve et al., 1987; Mark et al., 2014; Osinski, 2003; Osinski et al., 2004). This suggests a greater interaction with water than that of simple diffusion at ambient temperatures (Denton et al., 2009), forming hydrothermal alteration zones within the fractures with high chemical heterogeneity indicating multiple stages of hydration and secondary mineral growth (Garde et al., 2022; Mark et al., 2014) (Figure 7). Accordingly, a significant volatile component is present in both glassy melt rocks (Table 3). However, the nature of the volatile phase is unclear from EMP analysis alone, and a carbon phase (CO_2 or CO) could also be present, likely originating from carbonaceous material within the sample or the incorporation into the melt of small volumes of carbonate lithologies in the proposed target sequence.

In addition to the silicate-based melt sample, large fragments of vesicular siliceous glass within the carbonate samples (Figure 8) contain vesicle infill of crystalline carbonate that shows no elevations of Si and Al (Figure 9). Although these near-spherical calcite bodies optically resemble that of globular calcite spherules formed due to carbonate–silicate liquid immiscibly as seen in other impact craters, for example, quenched "splash-from" melt droplets incorporated into silicate breccias in the Ries crater, Germany (Graup, 1999), here a more likely explanation is that the spherical carbonate features in the glass fragment formed as a result of hydrothermally remobilized carbonate (Si-Al-poor),

originating from the carbonate melt and supplied through pervasive fractures within the glass fragments in a postimpact low-temperature hydrothermal setting.

Collectively these observations indicate either interaction of contained water, heterogeneously distributed within the melt upon formation, or infiltration of water during cooling and subsequent hydrothermal alteration, or both.

Organic Material

Organic matter in various states of preservation is observed within the melt rocks (Figure 10). Amorphous organic material in the hypocrystalline melt rocks is relatively sparse and is interpreted as having likely been incorporated directly into the melts and highly transformed. An alternative explanation is that organic material was introduced during postimpact hydrothermal activity, as suggested for the Gardnos impact crater, Norway (Lindgren et al., 2019). Wood fragments up to 2 cm across with well-preserved conifer-type cell structures are present within the carbonate-based melt rock HW19-39 and must have been incorporated directly as fragments. Observations of distorted cell structures and common shrinkage textures are likely due to rapid volatile loss from the carbonaceous material during heating (Garde et al., 2020). In addition, carbonaceous material in vesicular impact glass from sample HW19-32 indicates rapid heating and devolatilization of organic material, forming amorphous vesicles trapped within the melt (Figure 10d). The increased occurrence of carbonaceous material in the glassy and carbonate melt rocks is likely due to the short duration of the high-temperature excursions and more rapid cooling, in comparison to the more slowly cooled, hypocrystalline melt rocks where organic material is dispersed and sparser.

The significant amount of organic material embedded within the melt rocks requires that abundant organic matter was present in the target area at the time of impact in the Late Paleocene. There are no known organic-rich lithologies in the immediate foreland of the crater, such as shale or coal. However, during the Late Paleocene, the adjacent Ellesmere Island in Arctic Canada, <200 km from Inglefield Land, was covered in dense, high-latitude forestation dominated by redwoods (e.g., Williams et al., 2009) and much warmer than it is today. It is not unreasonable to infer that extensive forests probably also covered Greenland in the Late Paleocene. Garde et al. (2020) showed charcoal/lignite material sampled from the glaciofluvial floodplain, which was identified as remnants of mainly conifer wood interpreted to have formed by impact-induced wildfire. They also reported millimeter-sized carbonaceous particles with very high reflectance containing relict cell structures, as well as

dispersed organic matter in impact melt grains (Garde et al., 2022). These variable organic remains closely correspond to the material incorporated into the Hiawatha impactite rocks described here. Mantles of organic carbon on microlite phases were also described in previous studies (Garde et al., 2020, 2022; Kjær et al., 2018). The recent ~58 Ma U–Pb zircon age determination by Kenny et al. (2022) shows that the pre-impact area was ice-free (Silber et al., 2021), and that organic material incorporated in melts here is not derived from the most recent forestation in the Late Pliocene to Early Pleistocene, but was nevertheless formed by impacting into a hydrous terrestrial setting with abundant vegetation.

Further Evidence of an Iron Impactor at Hiawatha

Three Hiawatha melt rock samples, from both the hypocrystalline and glassy subgroups, show elevated PGE abundances when compared to UCC (McLennan, 1998; Park et al., 2012; Figure 13). It is well established that during hypervelocity impact of large extraterrestrial objects into terrestrial crust a fraction of the impactor may be incorporated into rocks that were once molten, that is, impact melt rocks (e.g., McDonald, 2002) via recondensation of the vaporized projectile, if the impact shock energy is sufficiently high (French & Koeberl, 2010; Koeberl et al., 2012) or, more rarely, by physical incorporation of partly molten or solid fragments into the impact melt if the energy is low enough for their survival (Hart et al., 2002; Maier et al., 2006; Potter & Collins, 2013). Anomalous PGE ratios observed in the PGE-enriched silicate melt rocks from the Hiawatha impact structure (averages of $[Rh/Pt]_N = 1.37$, $[Rh/Ru]_N = 0.32$ and $[Pd/Pt]_N = 3.23$) are unusual for terrestrial rocks, but common for fractionated iron meteorites. Terrestrial candidate sources for the origin of the high $(Rh/Pt)_N$ values are depleted mantle, some komatiitic lavas or rare sulfide-rich chromite rocks (Guice et al., 2019; Holwell & McDonald, 2006; Maier et al., 2003) with only the latter realistically likely to produce the accompanying high $(Rh/Os)_N$ and $(Rh/Ir)_N$ values. No occurrences of such lithologies are known from the exposed foreland adjacent to the Hiawatha impact structure (Nutman et al., 2008). Only minor occurrences of ultramafic rocks in association with marble (Etah Group paragneiss) are known (Figure 1a) and given their size and metamorphic origin, these would be unable volumetrically and compositionally to produce the observed PGE ratios in the melt rocks (Figure 13).

Kjær et al. (2018) analyzed three different samples of glaciofluvial sand from the Hiawatha impact structure for PGE concentrations. Two sand samples (HW12-2016 and HW13-2016), in which no impactite grains or shock

indicators (e.g., quartz grains with PDFs) were observed, contained low PGE abundances consistent with UCC, and were interpreted to be dominated by components from local bedrock and likely unaffected by the impact (Kjær et al., 2018). Significantly lower PGE abundances were recorded in two Hiawatha carbonate-based samples in this study (HW19-28 & HW19-39), which agrees with the non-impact-related sand (Figure 13) samples from Kjær et al. (2018), and therefore also reflect PGE-concentrations of the local crust. Although, sand sample (HW21-2016), rich in impact-derived melt grains (Garde et al., 2022), produced chondrite-normalized signatures similar to the PGE-enriched melt rocks analyzed here, at similar concentrations (Figure 13b). The PGE signature of this sand sample showed non-terrestrial PGE ratios ($[Rh/Pt]_N > 1.2$, $[Rh/Ru]_N < 0.3$ and $[Pd/Pt]_N > 2.5$) and was interpreted to be of an impactor origin (Kjær et al., 2018). However, the similar PGE abundances of the rock samples studied here and sand sample HW21-2016 infers that the PGE-enriched melt rocks studied here are unlikely to be the source rock of the HW21-16 sand, as the sand certainly also comprises sediment originating from outside the crater or non-melted areas of the structure. Therefore, a more PGE-enriched impact lithology, which incorporated a larger proportion of the impactor, is likely to have existed within the crater to produce the observed PGE-enriched signature in the sand.

A chondritic impactor is ruled out as it cannot produce the above-mentioned PGE ratios and fractionated siderophile element patterns of the magnitude seen in the HW21-2016 sand (Kjær et al., 2018). A highly fractionated iron meteorite (Duchesne IVA iron meteorite) impactor was proposed, based on it being the best candidate to reproduce the negative Pt anomalies and PGE signatures of the PGE-enriched HW21-2016. Applying the same reasoning, the same can be concluded for the PGE-enriched Hiawatha melt rocks which show similar PGE abundances and ratios.

CONCLUSIONS

- Pebble- to boulder-sized glaciofluvial rock samples collected along the margin of the Hiawatha impact structure contain diagnostic shocked minerals embedded in glassy to hypocrystalline impact melts, and further support an impact origin of the hidden structure.
- The matrix microlite assemblages and melt glass textures of the impact melt rocks for the first time display highly shocked minerals and fragments of

organic material located in situ inside impact melts and closely resemble those of previously studied sand grains from the proximal glaciofluvial floodplain (Garde et al., 2022).

- Analyzed PGE abundances and PGE ratios in the melt rock samples are similar to those previously found in glaciofluvial sand sample HW21-16 eroded from the crater and support the identification of a highly fractionated Fe-meteorite-related impactor (Kjær et al., 2018).
- Melt rock samples with a flow-textured carbonate matrix indicate that significant volumes of calcareous rocks were present within the target area, either marbles which form an integral part of the Paleoproterozoic Etah Group, or Franklinian, Cambrian–Ordovician shelf carbonates, such as presently exposed along the coast of Inglefield Land.
- Abundant organic material with occasional conifer-type cell structures preserved within the melt rocks is highly unusual and suggests that Inglefield Land was covered by a dense, high-latitude forest such as on adjacent Ellesmere Island in the Late Paleocene. The preservation states of these biosignatures appear to be good.
- Widespread hydrothermal alteration observed within the melt rock samples, including smectite crystallization, vesiculation, devitrification of glass, and formation of spherulites and carbonate remobilization, indicates multiple high- to low-temperature hydrothermal events, probably resembling both the initiation and later stages of a postimpact hydrothermal system, as well as the interaction with contained water within the melt.
- The study of impactites sampled from outside an impact crater (float samples) is argued for here, when clear topographical evidence for transportation from an impact structure is demonstrated. In the future, proposed impact crater discoveries beneath thick ice coverage via airborne surveys, that is, beneath the Greenland Ice Sheet or the Antarctic Ice Sheet, could be studied similarly and even dated.

REFERENCES

Bessette, J. T., Schroeder, D. M., Jordan, T. M., and MacGregor, J. A. 2021. Radar-Sounding Characterization of the Subglacial Groundwater Table beneath Hiawatha Glacier, Greenland. *Geophysical Research Letters* 48: 1–11. https://doi.org/10.1029/2020GL091432.

Clemens, J. D., and Wall, V. J. 1988. Controls on the Mineralogy of S-Type Volcanic and Plutonic Rocks. *Lithos* 21: 53–66. https://doi.org/10.1016/0024-4937(88)90005-9.

Dawes, P.R. 2004 Explanatory Notes to the Geological map of Greenland, 1:500 000, Humboldt Gletscher, Sheet 6, 1–48. https://doi.org/10.34194/geusm.v1.4615.

Dawes, P. R. 2009. Precambrian—Palaeozoic Geology of Smith Sound, Canada and Greenland: Key Constraint to Palaeogeographic Reconstructions of Northern Laurentia and the North Atlantic Region. *Terra Nova* 21: 1–13. https://doi.org/10.1111/j.1365-3121.2008.00845.x.

Dawes, P. R., Frisch, T., Garde, A. A., Iannelli, T. R., Ineson, J. R., Jensen, S. M., Pirajno, F., et al. 2000. Kane Basin 1999: Mapping, Stratigraphic Studies and Economic Assessment of Precambrian and Lower Palaeozoic Provinces in North-Western Greenland. *Geology of Greenland Survey Bulletin* 186: 11–28. https://doi.org/10.34194/ggub.v186.5211.

De Vos, E., Edwards, S. J., McDonald, I., Wray, D. S., and Carey, P. J. 2002. A Baseline Survey of the Distribution and Origin of Platinum Group Elements in Contemporary Fluvial Sediments of the Kentish Stour, England. *Applied Geochemistry* 17: 1115–21. https://doi.org/10.1016/S0883-2927(02)00010-0.

Denton, J. S., Tuffen, H., Gilbert, J. S., and Odling, N. 2009. The Hydration and Alteration of Perlite and Rhyolite. *Journal of the Geological Society* 166: 895–904. https://doi.org/10.1144/0016-76492008-007.

Dressler, B. O., and Reimold, W. U. 2001. Terrestrial Impact Melt Rocks and Glasses. *Earth Science Reviews* 56: 205–84.

French, B. M. 1998. *Traces of Catastrophe: A Handbook of Shock-Metamorphic Effects in Terrestrial Meteorite Impact Structures*. LPI Contribution No. 954, Lunar and Planetary Institute, Houston, TX, 120 pp. https://doi.org/10.1180/0026461026650059

French, B. M., and Koeberl, C. 2010. The Convincing Identification of Terrestrial Meteorite Impact Structures: What Works, What Doesn't, and Why. *Earth-Science Reviews* 98: 123–70. https://doi.org/10.1016/j.earscirev.2009.10.009.

French, B. M., Koeberl, C., Gilmour, I., Shirey, S. B., Dons, J. A., and Naterstad, J. 1997. The Gardnos Impact Structure, Norway: Petrology and Geochemistry of Target Rocks and Impactites. *Geochimica et Cosmochimica Acta* 61: 873–904. https://doi.org/10.1016/S0016-7037(96)00382-1.

Garde, A. A., Keulen, N., and Waight, T. 2022. Microporphyritic and Microspherulitic Melt Grains, Hiawatha Crater, Northwest Greenland: Implications for Post-Impact Cooling Rates, Hydration, and the Cratering Environment. *Geological Society of America Bulletin* 134: 2145–66. https://doi.org/10.1130/B36058.1.

Garde, A. A., Søndergaard, A. S., Guvad, C., Dahl-Møller, J., Nehrke, G., Sanei, H., Weikusat, C., Funder, S., Kjær, K. H., and Larsen, N. K. 2020. Pleistocene Organic Matter Modified by the Hiawatha Impact, Northwest Greenland. *Geology* 48: 867–71. https://doi.org/10.1130/G47432.1.

Graham, S., and Keulen, N. 2019. Nanoscale Automated Quantitative Mineralogy: A 200-Nm Quantitative Mineralogy Assessment of Fault Gouge Using Mineralogic. *Minerals* 9: 1–12. https://doi.org/10.3390/min9110665.

Graup, G. 1999. Carbonate-Silicate Liquid Immiscibility upon Impact Melting: Ries Crater, Germany. *Meteoritics & Planetary Science* 34: 425–38. https://doi.org/10.1111/j.1945-5100.1999.tb01351.x.

Grieve, R. A. F. 1975. Petrology and Chemistry of the Impact Melt at Mistastin Lake Crater, Labrador. *Bulletin of the Geological Society of America* 86: 1617–29. https://doi.org/10.1130/0016-7606(1975)86<1617:PACOTI>2.0.CO;2.

Grieve, R. A. F., Bottomley, R. B., Bouchard, M. A., Robertson, P. B., Orth, C. J., and Attrep, M. 1991. Impact Melt Rocks from New Quebec Crater, Quebec, Canada. *Meteoritics* 26: 31–9. https://doi.org/10.1111/j.1945-5100.1991.tb01012.x.

Grieve, R. A. F., Dence, M. R., and Robertson, R. B. 1997. Cratering Processes: As Interpreted from the Occurrence of Impact Melts. In *Impact and Explosion Cratering*, edited by D. J. Roddy, R. O. Pepin, and R. B. Merrill, 791–814. New York: Pergamon Press.

Grieve, R. A. F., Reny, G., Gurov, E. P., and Ryabenko, V. A. 1987. The Melt Rocks of the Boltysh Impact Crater, Ukraine, USSR. *Contributions to Mineralogy and Petrology* 96: 56–62. https://doi.org/10.1007/BF00375525.

Guice, G. L., McDonald, I., Hughes, H. S. R., and Anhaeusser, C. R. 2019. An Evaluation of Element Mobility in the Modderfontein Ultramafic Complex, Johannesburg: Origin as an Archaean Ophiolite Fragment or Greenstone Belt Remnant? *Lithos* 332–333: 99–119. https://doi.org/10.1016/j.lithos.2019.02.013.

Gupta, S. C., Love, S. G., and Ahrens, T. J. 2002. Shock Temperature in Calcite ($CaCO_3$) at 95-160 GPa. *Earth and Planetary Science Letters* 201: 1–12. https://doi.org/10.1016/S0012-821X(02)00685-4.

Gurov, E. P., and Koeberl, C. 2004. Shocked Rocks and Impact Glasses from the El'gygytgyn Impact Structure, Russia. *Meteoritics & Planetary Science* 39: 1495–508. https://doi.org/10.1111/j.1945-5100.2004.tb00124.x.

Gustafsson, J. 2020. Impactites from the Hiawatha Crater, North-West Greenland (Master thesis). Department of Geological Sciences, Stockholm University, 1–48.

Hart, R. J., Cloete, M., McDonald, I., Carlson, R. W., and Andreoli, M. A. G. 2002. Siderophile-Rich Inclusions from the Morokweng Impact Melt Sheet, South Africa: Possible Fragments of a Chondritic Meteorite. *Earth and Planetary Science Letters* 198: 49–62. https://doi.org/10.1016/S0012-821X(02)00497-1.

Higgins, A., Ineson, J., Peel, J., Surlyk, F., and Sønderholm, M. 1991. Lower Palaeozoic Franklinian Basin of North Greenland. *Bulletin Grønlands Geologiske Undersøgelse* 160: 71–139. https://doi.org/10.34194/bullggu.v160.6714

Holwell, D. A., and McDonald, I. 2006. Petrology, Geochemistry and the Mechanisms Determining the Distribution of Platinum-Group Element and Base Metal Sulphide Mineralisation in the Platreef at Overysel, Northern Bushveld Complex, South Africa. *Mineralium Deposita* 41: 575–98. https://doi.org/10.1007/s00126-006-0083-5.

Ineson, J. R., and Peel, J. S. 1987. Cambrian Platform—Outer Shelf Relationships in the Nordenskiöld Fjord Region, Central North Greenland. *Rapport Grønlands Geologiske Undersøgelse* 133: 13–26. https://doi.org/10.34194/rapggu.v133.7972.

Jaret, S. J., Kah, L. C., and Harris, R. S. 2014. Progressive Deformation of Feldspar Recording Low-Barometry Impact Processes, Tenoumer Impact Structure, Mauritania. *Meteoritics & Planetary Science* 49: 1007–22. https://doi.org/10.1111/maps.12310.

Jaret, S. J., Phillips, B. L., King, D. T., Glotch, T. D., Rahman, Z., and Wright, S. P. 2017. An Unusual Occurrence of Coesite at the Lonar Crater, India. *Meteoritics and Planetary Science* 52: 147–63. https://doi.org/10.1111/maps.12745.

Jochum, K. P., Stoll, B., Herwig, K., Willbold, M., Hofmann, A. W., Amini, M., Aarburg, S., et al. 2006. MPI-DING Reference Glasses for in Situ Microanalysis: New Reference Values for Element Concentrations and Isotope Ratios. *Geochemistry, Geophysics, Geosystems* 7: Q02008. https://doi.org/10.1029/2005GC001060.

Juvonen, R., Lakomaa, T., and Soikkeli, L. 2002. Determination of Gold and the Platinum Group Elements in Geological Samples by ICP-MS after Nickel Sulphide Fire Assay: Difficulties Encountered with Different Types of Geological Samples. *Talanta* 58: 595–603. https://doi.org/10.1016/S0039-9140(02)00330-2.

Kalleson, E., Dypvik, H., and Nilsen, O. 2010. Melt-Bearing Impactites (Suevite and Impact Melt Rock) Within the Gardnos Structure, Norway. *Meteoritics & Planetary Science* 45: 798–827. https://doi.org/10.1111/j.1945-5100.2010.01055.x.

Kenny, G. G., Hyde, W. R., Storey, M., and Garde, A. A. 2022. A Late Paleocene Age for Greenland's Hiawatha Impact Structure. *Science Advances* 8: eabm2434. https://doi.org/10.1126/sciadv.abm2434.

Kenny, G. G., Schmieder, M., Whitehouse, M. J., Nemchin, A. A., Morales, L. F. G., Buchner, E., Bellucci, J. J., and Snape, J. F. 2019. A New U-Pb Age for Shock-Recrystallised Zircon from the Lappajärvi Impact Crater, Finland, and Implications for the Accurate Dating of Impact Events. *Geochimica et Cosmochimica Acta* 245: 479–94. https://doi.org/10.1016/j.gca.2018.11.021.

Keulen, N., Malkki, S. N., and Graham, S. 2020. Automated Quantitative Mineralogy Applied to Metamorphic Rocks. *Minerals* 10: 47. https://doi.org/10.3390/min10010047.

Kieffer, S. W., and Simonds, C. H. 1980. The Role of Volatiles and Lithology in the Impact Cratering Process. *Reviews of Geophysics* 18: 143–81. https://doi.org/10.1029/RG018i001p00143.

Kieth, H. D., and Padden, F. J. 1963. A Phenomenological Theory of Spherulitic Crystallization. *Journal of Applied Physics* 34: 2409–21. https://doi.org/10.1063/1.1702757.

Kjær, K. H., Larsen, N. K., Binder, T., Bjørk, A. A., Eisen, O., Fahnestock, M. A., Funder, S., et al. 2018. A Large Impact Crater beneath Hiawatha Glacier in Northwest Greenland. *Science Advances* 4: 1–11. https://doi.org/10.1126/sciadv.aar8173.

Koeberl, C., Claeys, P., Hecht, L., and McDonald, I. 2012. Geochemistry of Impactites. *Elements* 8: 37–42. https://doi.org/10.2113/gselements.8.1.37.

Lange, M. A., and Ahrens, T. J. 1986. Shock-Induced CO_2 Loss from $CaCO_3$: Implications for Early Planetary Atmospheres. *Earth and Planetary Science Letters* 77: 409–18. https://doi.org/10.1016/0012-821X(86)90150-0.

Lindgren, P., Hallis, L., Hage, F. S., Lee, M. R., Parnell, J., Plan, A., Doye, A., and MacLaren, I. 2019. A TEM and EELS Study of Carbon in a Melt Fragment from the Gardnos Impact Structure. *Meteoritics & Planetary Science* 54: 2698–709. https://doi.org/10.1111/maps.13381.

Lodders, K. 2003. Solar System Abundances and Condensation Temperatures of the Elements. *The Astrophysical Journal* 591: 1220–47. http://stacks.iop.org/0004-637X/591/ia=1220.

Lofgren, G. 1971. Spherulitic Textures in Glassy and Crystalline Rocks. *Journal of Geophysical Research* 76: 5635–48. https://doi.org/10.1029/jb076i023p05635.

Lofgren, G. 1974. An Experimental Study of Plagioclase Crystal Morphology; Isothermal Crystallization. *American Journal of Science* 274: 243–73. https://doi.org/10.2475/ajs.274.3.243.

Mader, M. M., and Osinski, G. R. 2018. Impactites of the Mistastin Lake Impact Structure: Insights into Impact Ejecta Emplacement. *Meteoritics & Planetary Science* 53: 2492–518. https://doi.org/10.1111/maps.13173.

Maier, W. D., Andreoli, M. A., McDonald, I., Higgins, M. D., Boyce, A. J., Shukolyukov, A., Lugmair, G. W., et al. 2006. Discovery of a 25-cm Asteroid Clast in the Giant Morokweng Impact Crater, South Africa. *Nature* 441: 203–6. https://doi.org/10.1038/nature04751.

Maier, W. D., Roelofse, F., and Barnes, S. J. 2003. The Concentration of the Platinum-Group Elements in South African Komatiites: Implications for Mantle Sources, Melting Regime and PGE Fractionation During Crystallization. *Journal of Petrology* 44: 1787–804. https://doi.org/10.1093/petrology/egg059.

Mark, D. F., Lindgren, P., and Fallick, A. E. 2014. A High-Precision $^{40}Ar/^{39}Ar$ Age for Hydrated Impact Glass from the Dellen Impact, Sweden. *Geological Society of London, Special Publications* 378: 349–66. https://doi.org/10.1144/SP378.22.

McArthur, A. N., Cas, R. A. F., and Orton, G. J. 1998. Distribution and Significance of Crystalline, Perlitic and Vesicular Textures in the Ordovician Garth Tuff (Wales). *Bulletin of Volcanology* 60: 260–85. https://doi.org/10.1007/s004450050232.

McDonald, I. 1993. The Geochemical Behaviour of the Platinum-Group Elements in some Igneous Melts with an Accompanying Carbonaceous Volatile Phase, as Determined by Neutron Activation Analysis. University of Cape Town, 294.

McDonald, I. 2002. Clearwater East Impact Structure: A Re-interpretation of the Projectile Type Using New Platinum-Group Element Data from Meteorites. *Meteoritics & Planetary Science* 37: 459–64. https://doi.org/10.1111/j.1945-5100.2002.tb00828.x.

McDonald, I., and Viljoen, K. S. 2006. Platinum-Group Element Geochemistry of Mantle Eclogites: A Reconnaissance Study of Xenoliths from the Orapa Kimberlite, Botswana. *Transactions of the Institutions of Mining and Metallurgy, Section B: Applied Earth Science* 115: 81–93. https://doi.org/10.1179/174327506X138904.

McLennan, S. M. 1998. Composition of the Upper Continental Crust Revisited: Insights from Sedimentary Rocks. *Mineralogical Magazine* 62A: 983–4. https://doi.org/10.1180/minmag.1998.62a.2.182.

Nutman, A. P., Dawes, P. R., Kalsbeek, F., and Hamilton, M. A. 2008. Palaeoproterozoic and Archaean Gneiss Complexes in Northern Greenland: Palaeoproterozoic Terrane Assembly in the High Arctic. *Precambrian Research* 161: 419–51. https://doi.org/10.1016/j.precamres.2007.09.006.

Osinski, G. R. 2003. Impact Glasses in Fallout Suevites from the Ries Impact Structure, Germany: An Analytical SEM Study. *Meteoritics and Planetary Science* 38: 1641–67. https://doi.org/10.1111/j.1945-5100.2003.tb00006.x.

Osinski, G. R. 2004. Impact Melt Rocks from the Ries Structure, Germany: An Origin as Impact Melt Flows? *Earth and Planetary Science Letters* 226: 529–43. https://doi.org/10.1016/j.epsl.2004.08.012.

Osinski, G. R. 2007. Impact Metamorphism of $CaCO_3$-Bearing Sandstones at the Haughton Structure, Canada. *Meteoritics and Planetary Science* 42: 1945–60. https://doi.org/10.1111/j.1945-5100.2007.tb00552.x.

Osinski, G. R., Grieve, R. A. F., Bleacher, J. E., Neish, C. D., Pilles, E. A., and Tornabene, L. L. 2018. Igneous Rocks Formed by Hypervelocity Impact. *Journal of Volcanology and Geothermal Research* 353: 25–54. https://doi.org/10.1016/j.jvolgeores.2018.01.015.

Osinski, G. R., Grieve, R. A. F., Collins, G. S., Marion, C., and Sylvester, P. 2008. The Effect of Target Lithology on the Products of Impact Melting. *Meteoritics & Planetary Science* 43: 1939–54. https://doi.org/10.1111/j.1945-5100.2008.tb00654.x.

Osinski, G. R., Grieve, R. A. F., Ferrière, L., Losiak, A., Pickersgill, A. E., Cavosie, A. J., Hibbard, S. M., et al. 2022. Impact Earth: A Review of the Terrestrial Impact Record. *Earth-Science Reviews* 232: 104112. https://doi.org/10.1016/j.earscirev.2022.104112.

Osinski, G. R., Grieve, R. A. F., and Spray, J. G. 2004. The Nature of the Groundmass of Surficial Suevite from the Ries Impact Structure, Germany, and Constraints on its Origin. *Meteoritics & Planetary Science* 39: 1655–83. https://doi.org/10.1111/j.1945-5100.2004.tb00065.x.

Osinski, G. R., and Spray, J. G. 2001. Impact-Generated Carbonate Melts: Evidence from the Haughton Structure, Canada. *Earth and Planetary Science Letters* 194: 17–29. https://doi.org/10.1016/S0012-821X(01)00558-1.

Osinski, G. R., Spray, J. G., and Grieve, R. A. F. 2008. Impact Melting in Sedimentary Target Rocks: An Assessment. *Special Paper of the Geological Society of America* 437: 1–18. https://doi.org/10.1130/2008.2437(01).

Osinski, G. R., Spray, J. G., and Lee, P. 2005. Impactites of the Haughton Impact Structure, Devon Island, Canadian High Arctic. *Meteoritics & Planetary Science* 40: 1789–812. https://doi.org/10.1111/j.1945-5100.2005.tb00147.x.

Osinski, G. R., Tornabene, L. L., Banerjee, N. R., Cockell, C. S., Flemming, R., Izawa, M. R. M., McCutcheon, J., et al. 2013. Impact-Generated Hydrothermal Systems on Earth and Mars. *Icarus* 224: 347–63. https://doi.org/10.1016/j.icarus.2012.08.030.

Park, J. W., Hu, Z., Gao, S., Campbell, I. H., and Gong, H. 2012. Platinum Group Element Abundances in the Upper Continental Crust Revisited—New Constraints from Analyses of Chinese Loess. *Geochimica et Cosmochimica Acta* 93: 63–76. https://doi.org/10.1016/j.gca.2012.06.026.

Pirajno, F. 2005. Hydrothermal Processes Associated with Meteorite Impact Structures: Evidence from Three Australian Examples and Implications for Economic Resources. *Australian Journal of Earth Sciences* 52: 587–605. https://doi.org/10.1080/08120090500170468.

Potter, R. W. K., and Collins, G. S. 2013. Numerical Modeling of Asteroid Survivability and Possible Scenarios for the Morokweng Crater-Forming Impact. *Meteoritics & Planetary Science* 48: 744–57. https://doi.org/10.1111/maps.12098.

Schmieder, M., and Jourdan, F. 2013. The Lappajärvi Impact Structure (Finland): Age, Duration of Crater Cooling, and Implications for Early Life. *Geochimica et Cosmochimica Acta* 112: 321–39. https://doi.org/10.1016/j.gca.2013.02.015.

Sharp, T. G., and DeCarli, P. S. 2006. Shock Effects in Meteorites. In *Meteorites and the Early Solar System II*, edited by D. S. Lauretta and H. Y. McSween Jr., 653–77. Tucson: University of Arizona Press. http://www.lpi.usra.edu/books/MESSII/9040.pdf.

Silber, E. A., Johnson, B. C., Bjonnes, E., MacGregor, J. A., Larsen, N. K., and Wiggins, S. E. 2021. Effect of Ice Sheet Thickness on Formation of the Hiawatha Impact Crater. *Earth and Planetary Science Letters* 566: 116972. https://doi.org/10.1016/j.epsl.2021.116972.

Stöffler, D. 1984. Glasses Formed by Hypervelocity Impact. *Journal of Non-Crystalline Solids* 67: 465–502. https://doi.org/10.1016/0022-3093(84)90171-6.

Stöffler, D., Artemieva, N. A., Wünnemann, K., Reimold, W. U., Jacob, J., Hansen, B. K., and Summerson, I. A. T. 2013. Ries Crater and Suevite Revisited-Observations and Modeling Part I: Observations. *Meteoritics & Planetary Science* 48: 515–89. https://doi.org/10.1111/maps.12086.

Stöffler, D., Hamann, C., and Metzler, K. 2018. Shock Metamorphism of Planetary Silicate Rocks and Sediments: Proposal for an Updated Classification System. *Meteoritics & Planetary Science* 53: 5–49. https://doi.org/10.1111/maps.12912.

Stöffler, D., and Langenhorst, F. 1994. Shock Metamorphism of Quartz in Nature and Experiment: I. Basic Observation and Theory. *Meteoritics & Planetary Science* 29: 155–81. https://doi.org/10.1111/j.1945-5100.1994.tb00670.x.

Timms, N. E., Erickson, T. M., Pearce, M. A., Cavosie, A. J., Schmieder, M., Tohver, E., Reddy, S. M., Zanetti, M. R., Nemchin, A. A., and Wittmann, A. 2017. A Pressure-Temperature Phase Diagram for Zircon at Extreme Conditions. *Earth-Science Reviews* 165: 185–202. https://doi.org/10.1016/j.earscirev.2016.12.008.

Walton, E. L., Timms, N. E., Hauck, T. E., MacLagan, E. A., and Herd, C. D. K. 2019. Evidence of Impact Melting and

Post-Impact Decomposition of Sedimentary Target Rocks from the Steen River Impact Structure, Alberta, Canada. *Earth and Planetary Science Letters* 515: 173–86. https://doi.org/10.1016/j.epsl.2019.03.015.

Whitehead, J., Grieve, R. A. F., and Spray, J. G. 2002. Mineralogy and Petrology of Melt Rocks from the Popigai Impact Structure, Siberia. *Meteoritics & Planetary Science* 37: 623–47. https://doi.org/10.1111/j.1945-5100.2002.tb00844.x.

Whitehead, J., Spray, J. G., and Grieve, R. A. F. 2002. Origin of "Toasted" Quartz in Terrestrial Impact Structures. *Geology* 30: 431–4. https://doi.org/10.1130/0091-7613(2002)030<0431:OOTQIT>2.0.CO;2.

Williams, C. J., LePage, B. A., Johnson, A. H., and Vann, D. R. 2009. Structure, Biomass, and Productivity of a Late Paleocene Arctic Forest. *Proceedings of the Academy of Natural Sciences of Philadelphia* 158: 107–27. https://doi.org/10.1635/053.158.0106.

Wünnemann, K., Collins, G. S., and Osinski, G. R. 2008. Numerical Modelling of Impact Melt Production in Porous Rocks. *Earth and Planetary Science Letters* 269: 530–9. https://doi.org/10.1016/j.epsl.2008.03.007.

SUPPORTING INFORMATION

Additional supporting information may be found in the online version of this article.

Figure S1. Photomicrographs (plane-polarized light, PPL: cross-polarized light, XPL) of probable lithic impact breccias.

Figure S2. (a) Mineral-indexed AQM map of checkerboard feldspar clast adjacent to quartz clasts within hypocrystalline melt rock HW19-04. Checkerboard feldspar contains micrometer-scale subdomains of plagioclase surrounded by amorphous siliceous and K-feldspar glass. Rim of K-feldspar glass separates the two clasts. Note partially assimilated quartz clasts with coronas of orthopyroxene and biotite. (b) BSE image of same area. (c) Photomicrograph (PPL) of same area. Note highly toasted appearance of quartz and two cross-cutting sets of PDFs. (d–g) Element composition AQM maps (wt%) of checkerboard feldspar with plagioclase subdomains (Na: e) and siliceous and K-feldspar glass (K and Si: d and f).

Figure S3. (a) Photomicrograph (PPL) of thermally decomposed dark brown glass fragment with numerous vesicles in hypocrystalline matrix of sample HW19-04. Box shows the location of image (b). (b) Mineral-indexed AQM map of vesiculated (arrows) feldspathic glass fragment with variable composition, including regions of glass and kaolinite. Vesicles contain exsolved, zoned K-feldspar (exterior) and siliceous glass (center). Plagioclase microlites in the melt matrix appear to nucleate from the edge of the fragment. Box shows the location of images (c–j). (c) BSE image of glass fragment. Not brighter particles in the glass resembling higher Fe content (Fe: d). (d–j) SEM-EDS element composition maps (wt%) of same area showing highly variable composition of the glass fragment and vesicles.

Figure S4. Photomicrographs (plane-polarized light, PPL) and backscattered electron (BSE) images of zircon grains within melt rocks.

Figure S5. Photomicrographs of glassy melt rock sample HW19-32. (a, b) Centimeter-sized polycrystalline rock fragment containing mineral melts with flow structures and vesicles. Image (b) shows the variable isotropic nature of the mineral glasses. (c) Fragment of schlieric glass with distorted vesicles. (d, e) Shock-deformed feldspar of unknown composition, with alternate twin deformation (Jaret et al., 2014) displaying inclined lamellae and isotropization alternating between original twins.

Figure S6. (a) Mineral-indexed AQM map of sample HW19-39 displaying incomplete homogenization between bulk glass and feldspathic mineral glasses originating from millimeter-sized polycrystalline fragment. Glass shows highly variable compositions. (b) BSE showing new spherulite growth between the contact of the mineral glass and the bulk glass. Note internal decomposition structures and absorption of quartz in the decomposing quartz clast. (c) Plane light image of thin section showing location of zoomed area. (d–j) Element composition AQM (wt%). All images show the highly variable composition of the glasses.

Figure S7. Photomicrographs of shocked quartz grains with PDFs from two carbonate melt rock samples.

Table S1. Supplementary file (Excel) containing EMP analysis data.

Table S2. Supplementary file (Excel) containing PGE analysis data.

Table S3. Petrographic descriptions of 13 samples tentatively classified as lithic impact breccias.